Title
Unsaturated Flow Processes and the Onset of Seasonal Deformation in Slow-Moving Landslides

Journal
Journal of Geophysical Research Earth Surface, 126(5)

ISSN
2169-9003

Authors
Finnegan, NJ
Perkins, JP
Nereson, AL
et al.

Publication Date
2021-05-01

DOI
10.1029/2020jf005758

Unsaturated flow processes and the onset of seasonal deformation in slow-moving landslides

N. J. Finnegan[1], J. P. Perkins[2], A. L. Nereson, [3] and A. L. Handwerger[4,5]

[1]UC Santa Cruz, Department of Earth and Planetary Sciences, Santa Cruz, CA 95064

[2]U.S. Geological Survey, Geology, Minerals, Energy, and Geophysics Science Center, Moffett Field, CA 94035

[3]U.S. Geological Survey, Pacific Coastal and Marine Science Center, Santa Cruz, CA 95060

[4]Joint Institute for Regional Earth System Science and Engineering, University of California, Los Angeles, CA 90095

[5]Jet Propulsion Laboratory, California Institute of Technology, Pasadena, CA 91109

Corresponding author: Noah Finnegan (nfinnega@ucsc.edu)

Key Points:

- Vadose zone properties, especially thickness, modulate the style and timing of landslide pore pressure response to seasonal rainfall
- Field monitoring of a large, slow-moving landslide confirms acceleration in response to rainfall depends strongly on saturation state and hence rainfall history
- The onset of landslide motion can be cast as a rainfall intensity-duration threshold using knowledge of landslide material and hydraulic properties

Abstract

Predicting rainfall-induced landslide motion is challenging because shallow groundwater flow is extremely sensitive to the preexisting moisture content in the ground. Here, we use groundwater hydrology theory and numerical modeling combined with five years of field monitoring to illustrate how unsaturated groundwater flow processes modulate the seasonal pore water pressure rise and therefore the onset of motion for slow-moving landslides. The onset of landslide motion at Oak Ridge earthflow in California's Diablo Range occurs after an abrupt water table rise to near the landslide surface 52-129 days after seasonal rainfall commences. Model results and theory suggest that this abrupt rise occurs from the advection of a nearly saturated wetting front, which marks the leading edge of the integrated downward flux of seasonal rainfall, to the water table. Prior to this abrupt rise, we observe little measured pore water pressure response within the landslide due to rainfall. However, once the wetting front reaches the water table, we observe nearly instantaneous pore water pressure transmission within the landslide body that is accompanied by landslide acceleration. We cast the timescale to reach a critical pore water pressure threshold using a simple mass balance model that considers variable moisture storage with depth and explains the onset of seasonal landslide motion with a rainfall intensity-duration threshold. Our model shows that the seasonal response time of slow-moving landslides is controlled by the dry season vadose zone depth rather than the total landslide thickness.

Plain Language Summary

Landslides are often triggered by rainfall events that increase water pressure within rock and soil. A key impediment to predicting landslide motion is that movement of water in the ground is extremely sensitive to preexisting moisture content. Hence, rainfall history exerts a strong control on water movement into the ground. For large landslides, it is commonly assumed that the ground is saturated to the surface, which simplifies modeling of pressure changes. Here we show, however, that the dynamics of infiltration through unsaturated ground at the start of the wet season fundamentally control both the style and timing of landslide response to rainfall, which we verify through field monitoring of a large, slow-moving landslide in the California Coast Range. At the start of the wet season, we observe no pressure response at depth for weeks to months. However, eventually a sudden pore pressure rise in the landslide body marks the shift to a regime where pressure transmission and landslide acceleration from rainfall is nearly instantaneous. This bimodal behavior, which we can predict by comparing the seasonal rainfall rate to the unsaturated groundwater velocity, is an expected consequence of infiltration into initially unsaturated ground with the material properties observed.

1.0 Introduction and Background

Landslides, whether in rock or soil, occur when slope-parallel shear stresses acting in the downhill direction are greater than or equal to the shear strength resisting sliding within a hillslope. Assuming Coulomb friction, this condition is met when

$$\frac{\boldsymbol{\tau}}{(\boldsymbol{\sigma}-\boldsymbol{p})\tan\boldsymbol{\varphi}+\boldsymbol{c'}} \geq 1 \qquad (1)$$

where τ is slope-parallel shear stress, σ is the slope-normal stress, p is pore water pressure, φ is the friction angle (and $tan\varphi$ is the static coefficient of friction) and c' is effective cohesion. Instability in hillslopes is most commonly triggered either by co-seismic shaking, which can cause slope-parallel accelerations and increase pore water pressure (e.g., Jibson, 2007; Newmark, 1965), or by rainfall or snowmelt events that increase pore water pressure and therefore reduce effective normal stresses (defined as $\sigma - p$) and hence Coulomb friction (Iverson, 2000; Terzaghi, 1943). For the latter class of landslides, failure is therefore controlled by the evolution of pore water pressure in both space (e.g., Perkins et al., 2017; Reid & Iverson, 1992) and time (e.g., Iverson, 2000; Reid, 1994).

In this paper our objective is first to exploit a well-instrumented, large, deep-seated, slow-moving landslide that experiences both seasonal motion and seasonally-unsaturated conditions to understand how rainfall infiltration through the vadose zone controls the pore water pressure and deformation response of large landslides, and second, to explore generally how the combination of vadose zone thickness and material properties in a landslide govern the timing and magnitude of the seasonal piezometric response. Our motivation for this work is that large, deep-seated, slow-moving landslides, which are often referred to as earthflows (Hungr et al., 2014; Keefer & Johnson, 1983; Lacroix et al., 2020), play a fundamental role in the development of topographic relief (Mackey & Roering, 2011), the delivery of sediment to river channels (Finnegan et al., 2019; Mackey & Roering, 2011; Roering et al., 2015; Simoni et al., 2013), and the evolution of drainage networks (Bennett et al., 2016a; Shobe et al., 2020). In addition, earthflows represent a chronic source of damage to infrastructure such as railroads, utility pipelines, and highways (e.g., Alberti et al., 2020; Merriam, 1960). Thus it is important to develop and apply models that can be used to better understand landslide behavior.

Some slow-moving landslides exhibit an approximate pore pressure threshold for motion that is consistent with the model summarized in equation 1 (Corominas et al., 2005; Iverson & Major, 1987; Macfarlane, 2009; Schulz & Wang, 2014), while others exhibit a clear coupling between pore pressure and velocity above a threshold (Coe et al., 2003; Corominas et al., 2005; Malet et al., 2002). These mechanical-hydrologic relationships are often characterized by hysteresis in the relationship between pore pressure and velocity (van Asch et al., 2007; Carey et al., 2015; Massey et al., 2013) or an offset between the pore pressure threshold associated with the onset and cessation of motion (e.g., Priest et al., 2011). However, in other cases there is no obviously identifiable pressure threshold associated with the onset of motion (Angeli et al., 1996; Matsuura et al., 2003; Pyles et al., 1987; Schulz et al., 2018; Shibasaki et al., 2016). For these latter cases, as well as for cases with hysteresis between velocity and pore pressure, explanations for decoupling between pore pressure and deformation include 1) velocity-dependent shear strength (van Asch et al., 2007; Angeli et al., 1996); 2) snow loading that changes effective normal stresses (Matsuura et al., 2003); 3) Temperature-dependent shear strength (Shibasaki et al., 2016); 4) Clay swelling that increases lateral boundary friction during periods of high pore pressure (Schulz et al., 2018); and, 5) The superposition of different deformation mechanisms with distinct sensitivities to pore pressure (Massey et al., 2013). Indeed, how and why apparently stable frictional sliding in landslides occurs due to rising pore water pressures remains a fundamental problem in geomorphology and natural hazards research (Agliardi et al., 2020; Baum & Johnson, 1993; Carey et al., 2019; Carrière et al., 2018; Handwerger et al., 2016; Iverson, 2005; Wang et al., 2010).

While these effects suggest that predicting the motion of slow-moving landslides is complicated by evolving material properties and feedbacks between deformation and pore water pressure, among other factors, pore water pressure changes, nevertheless, remain a key trigger for landslide failure (Bogaard & Greco, 2016; Iverson, 2000). Consequently, notwithstanding the aforementioned complications, predicting pore water pressure changes remains a basic goal of landslide modeling and mitigation (e.g., Baum et al., 2008; Berti & Simoni, 2010, 2012; Iverson, 2000, 2005).

Towards that end, the simplest and most commonly used approach to modeling the evolution of pore water pressure in response to vertical infiltration of precipitation is via an approximation of complete saturation and 1-dimensional (1D) vertical linear diffusion (Iverson, 2000; Reid, 1994) such that

$$\partial p/_{\partial t} = D_o \partial^2 p/\partial z^2 \quad , \tag{2}$$

where p is pressure head (m), z is depth (m) below the surface, and D_o is hydraulic diffusivity (m^2/s). The 1D assumption implicit in equation (2) is justified by the much longer time scale of the lateral diffusion of pore water pressure relative to vertical in most landslides (Iverson, 2000). The assumption of linearity in equation (2) means that the characteristic response time of a landslide to rainfall infiltration can be estimated for a given landslide depth and hydraulic diffusivity, defined as $\tau_d = z^2 / D_o$ (Iverson, 2000). For this reason, analyses that link temporal patterns of rainfall and seasonal landslide deformation commonly adopt the model summarized in equation (2) (Cohen-Waeber et al., 2018; Handwerger et al., 2013, 2019; Hu et al., 2019, 2020; Iverson & Major, 1987; Schulz et al., 2009, 2017). However, the model described above does not allow for the possibility of an unsaturated zone above the water table through which rainfall would have to infiltrate. Therefore, while equation (2) is useful for understanding pore water pressure evolution in an already-saturated landslide, it cannot be used for predicting the early-season pore water pressure rise that accompanies the onset of motion in a seasonally-unsaturated landslide.

The presence of unsaturated ground above the water table is relevant to landslides because they are not saturated year-round, especially in landslide-prone areas with seasonal rainfall. In unsaturated ground, capillary forces within pores are able to hold centimeters to meters of saturated pore water pressure equivalent against gravity (e.g., Gillham, 1984). Hence, the rate of vertical infiltration of rainfall into the vadose zone should depend strongly on the antecedent near-surface moisture content (e.g., Bogaard & Greco, 2016), as has been shown for shallow landslides that are restricted to the soil mantle (Torres et al., 1998). Under unsaturated conditions the rate of change of moisture in the ground is governed by the Richardson-Richards equation (Richards, 1931; Richardson, 1922), which in the 1D “mixed water content form” (Ogden et al., 2017) is defined as

$$\frac{\partial \theta}{\partial t} = \frac{\partial}{\partial z}\left[K(\theta)\left(\frac{\partial \psi(\theta)}{\partial z} - 1\right)\right] \quad , \tag{3}$$

where $K(\theta)$ and $\psi(\theta)$ are the hydraulic conductivity (*m/s*) and soil hydraulic capillary head (*m*), respectively, both of which vary strongly with dimensionless moisture content (θ). Ogden et al. (2017) recast equation 3 as a Soil Moisture Velocity Equation that describes the rate at which a wetting front propagates vertically through an unsaturated medium:

$$\frac{\partial Z_R}{\partial t} = -K'(\theta)\left[\frac{\partial \psi(\theta)}{\partial z} - 1\right] - D(\theta)\frac{\partial^2\psi/\partial z^2}{\partial \psi/\partial z} \qquad (4)$$

where Z_R is the vertical position of the wetting front, $K'(\theta)$ is the vertical gradient of hydraulic conductivity at the wetting front, and D is the soil (or more generally, matrix) water diffusivity. The two terms of this equation represent the advective (left term) and diffusive (right term) modes of water transport in the vadose zone, which provide a convenient framework for considering their relative effects in delivering rainfall to a landslide water table leading to a rise in pore water pressure. Ogden et al. (2017) discuss the conditions under which the diffusive term of the soil moisture velocity equation is negligible. For example, in the case of a sharp wetting front, the vertical gradient of matric pressure $\partial\psi/\partial z$ is high, causing the denominator to become large and the diffusive term to vanish. Conversely, then, decreasing $\partial\psi/\partial z$ through progressive wetting of the vadose zone will cause the diffusive term to increase as the advective term decreases. Additionally, they show that if the vertical gradient of moisture content $\partial\theta/\partial z$ is constant in time – in other words, if the wetting front shape remains constant during infiltration – then the numerator of the diffusive term will be zero and the term will also vanish. Both of these instances suggest that infiltration into relatively dry ground, as in the case of early season infiltration into seasonally deforming landslides, should be dominated by the advective transport of pore water.

Observations of rainfall and pore water pressure or water table changes at numerous slow-moving landslides suggest that vadose zone processes (Berti & Simoni, 2010; Bogaard & van Asch, 2002; Malet et al., 2005; Osawa et al., 2018), including fracture flow (Krzeminska et al., 2013; Shao et al., 2016), are a key control on pore water pressure evolution. Additionally, in California, USA, where there is a Mediterranean climate characterized by hot, dry summers and cool, wet winters, the response of slow landslide velocities to the onset of winter rainfall can be between weeks and months (Cohen-Waeber et al., 2018; Handwerger et al., 2013, 2019; Iverson & Major, 1987), whereas measurements of the vertical propagation of groundwater pressure pulses under saturated conditions in otherwise similar clay-rich landslides reveal rapid pressure transmission in days to hours (Berti & Simoni, 2010; Corominas et al., 2005; Reid, 1994). Because early season rainfall would need to infiltrate through unsaturated ground at the landslide surface, it is expected that the early season response of a deep landslide to rainfall following a long dry period would be slow relative to when pore spaces were closer to saturation in the vadose zone. That said, we also acknowledge that for shallow landslides confined to the soil mantle, desiccation cracking may extend to the landslide base, leading to rapid early season piezometric responses to rainfall before cracks anneal in the winter (Collins et al., 2012).

The timing and pattern of early season landslide response therefore depends strongly on the antecedent moisture content, the hydraulic characteristics of the slide body, and the rate of water delivery from the surface. For example, a slow-moving bedrock landslide with a high bulk hydraulic conductivity (either through a porous matrix or strong contribution from secondary flow through macropores or fractures) may be able to quickly transmit individual rainfall pulses down to the water table (e.g., Xu et al., 2020), whereas a landslide with lower hydraulic conductivity may integrate many storm events into a single pulse that quickly drives up pore water pressures upon meeting the water table (e.g., Baum & Reid, 1992). To quantitatively characterize the style of rainfall delivery to the water table, we can compare the rate of rainfall infiltration into the ground from the ground surface to that of the wetting front propagation into unsaturated ground once rainfall has ceased. An approximation of the rainfall wetting front propagation rate from the ground surface can be derived from considering the mass balance of the rainfall flux and the fillable pore space in the unsaturated landslide body:

$$\frac{dz_r}{dt} = q_r/(\theta_s - \theta_i) \qquad (5),$$

where q_r is the rainfall flux (*m/s*) that is able to infiltrate into the ground, θ_s is the saturated moisture content, and θ_i is the initial moisture content (e.g., Baum & Reid, 1992; Bouwer, 1978). While strictly valid only until ponded conditions are reached, equation (5) nevertheless provides a useful estimate of initial wetting front velocity.

Similarly, the initial velocity of a wetting front into unsaturated ground after rainfall cessation can be approximated from a solution of the Soil Moisture Velocity Equation for what the authors call "falling slugs" (e.g., Ogden et al., 2015):

$$\frac{ds}{dt} = (K_s - K_i)/(\theta_s - \theta_i), \qquad (6)$$

where K_s and K_i are the respective hydraulic conductivities at θ_s and θ_i. Although in the absence of rainfall, wetting fronts tend to thin in the theta direction which changes their velocity (Ogden et al., 2015), equation (6) provides a general description of the initial advance of a wetting front following rainfall cessation. Hence, we can then define a quantity, that we term the "pulsivity" (P) of the moisture delivery, as the ratio of the falling slug velocity relative to the rainfall wetting front velocity, which simplifies to

$$P = (K_s - K_i)/q_r \qquad (7)$$

Pulsivity values >> 1 imply that water in the vadose zone can fall more quickly between rainstorms than the downward propagation rate from the rainfall infiltration front, so rainfall delivery to the water table should occur in discrete events associated with individual rainstorms. Pulsivities closer to 1 imply that the propagation of the wetting front into the ground cannot outpace the downward rainfall flux from the surface, so rainfall will build up behind the wetting front, leading to the formation of a single inverted water table that forms above but eventually meets the groundwater table. Another way of conceptualizing the pulsivity is that for P >> 1 pore water pressure rise is limited by rainfall delivery, whereas for pulsivity values close to 1, pore water rise is limited by the rate of downward propagation of the moisture front through the vadose zone.

In a similar vein, we can estimate the likelihood that an individual rainfall event will be able to fully connect to a landslide's shallow water table. Considering the total rainfall depth of a given storm, r_d (multiplying q_r by the storm duration Δt), we can solve equation (5) to estimate a coarse infiltration depth as $Z_i = r_d/(\theta_s - \theta_i)$. Taking the ratio of the infiltration depth relative to the water table depth d_{wt}, we define the storm surface-water table connectivity as

$$c_s = r_d/(d_{wt}(\theta_s - \theta_i)) \qquad (8)$$

Connectivity values < 1 imply that an infiltration front incorporating water for a given storm does not fully reach the water table at depth. In the case of early season rainfall, where the water table may be a few meters below the surface and the upper landslide body is dry (i.e., θ_i is small), the connectivity is low (< 1). Once the vadose zone is sufficiently wet into the rainy season, the storage $(\theta_s - \theta_i)$ is greatly reduced, and therefore the connectivity should greatly increase for an individual storm event as wetting fronts will propagate deeper for a given rainfall depth. Landslides with low early-season pulsivity and low early-season connectivity should therefore respond in a bimodal fashion, where the initial delivery of water comes as an inverted water table from the surface, saturating the entire slide body and leading to a large and rapid initial spike in pore water pressure. Once the landslide water table is near the surface, the connectivity should be near or exceeding a value of 1, and the landslide should respond at depth to individual rainfall events until the connectivity drops below 1.

In order to test the predictions of the conceptual and analytical framework established above, we exploit a well instrumented, slow-moving landslide that experiences seasonal unsaturated conditions to explore how rainfall infiltration through the vadose zone modulates the pore water pressure and landslide deformation. In particular, we choose a location where the vadose zone is thin (< 3 m) and developed in fine-grained, weathered rock. This combination of factors should, according to the framework established above, likely lead to a delayed, but large and bimodal pore pressure response following the onset of winter rainfall.

1.1 Oak Ridge Earthflow Study Locale

Oak Ridge earthflow is a seasonally-active landslide located in the northern Diablo Range, 40 km southeast of San Francisco, California (Figures 1a,c). Positioned on the south-facing flank of Oak Ridge, it extends 1.35 km in the horizontal direction from ridge top to near the valley bottom, spans about 400 m of vertical relief, and has an average slope of 15°. The landslide body is composed of Franciscan mélange, an assemblage of variably deformed and metamorphosed rock units formed in a subduction zone during the Mesozoic and early Cenozoic eras (Wakabayashi, 1992). At Oak Ridge, as is typical of the Franciscan mélange, the matrix is dominated by clay and silt (Nereson et al., 2018) but contains blocks of harder lithologies, including sandstone, chert and greenstone, that range widely in size. Soil cover is usually very thin (~10 cm) on the mélange. For this reason, the unsaturated flow processes described in this paper apply not to the soil, but rather to the seasonally unsaturated weathered rock above the water table, also referred to as the critical zone, in which there can be a large reservoir of rock moisture (Rempe & Dietrich, 2018).

The vadose zone structure at Oak Ridge is typical of Franciscan mélange (Hahm et al., 2019), with a thin (< 3 m) seasonally unsaturated zone of weathered mudstone mélange above perennially saturated, unweathered mudstone mélange. The matrix of unweathered Franciscan mélange typically exhibits a combination of low shear strength ($\Phi = 12\text{-}14^{\circ}$) (Nereson et al., 2018; Roadifer et al., 2009) and low field-scale hydraulic conductivity, $10^{-6}\text{-}10^{-10}$ m/s (Iverson and Major, 1987).

Precipitation at Oak Ridge earthflow falls almost-exclusively as rain between the months of October and May (PRISM Climate Group, 2017). This supports a mix of open oak savanna (~70% coverage) with some oak woodland (25%) at lower elevations. Additional details of the field location and deformation history for Oak Ridge earthflow are provided in Nereson and Finnegan (2019) and Nereson et al. (2018). Despite its name and appearance, Oak Ridge earthflow, like most earthflows in California (Keefer & Johnson, 1983; Schulz et al., 2018), moves primarily via sliding along a discrete failure surface rather than through internal deformation (Nereson & Finnegan, 2019). Shallow electrical resistivity tomography (ERT)

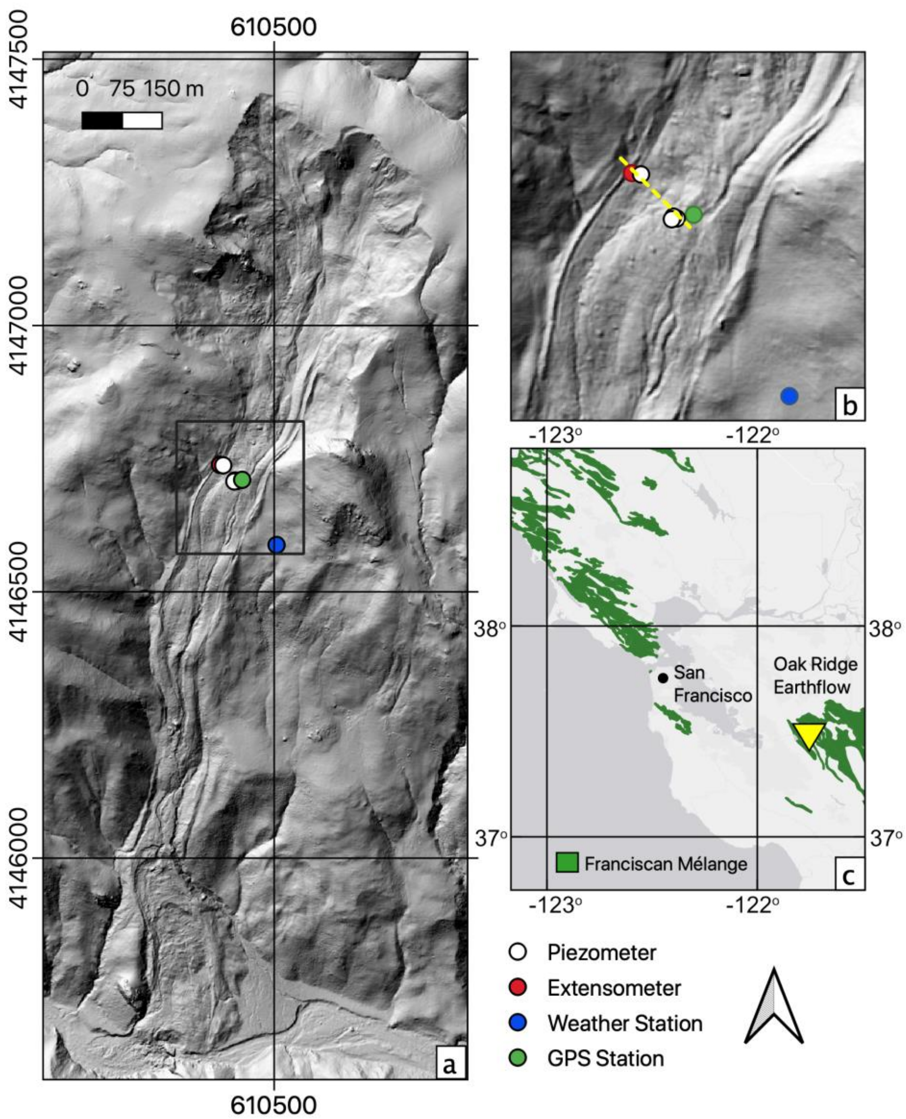

Figure 1. Oak Ridge earthflow, California, USA. a) lidar-generated shaded relief image of Oak Ridge earthflow. X and Y coordinates represent UTM Zone 10N easting and northing. b) Blow up of the region within the black box in a) showing the locations of instruments used in this study as well as the location of the cross-section shown (yellow dashed line) shown in Figure 2d. c) Location map of Oak Ridge earthflow showing the outcrop area of the Franciscan mélange. X and Y coordinates represent longitude and latitude

surveys at Oak Ridge suggest that the depth to the basal detachment at the location of the monitoring infrastructure described below is 8 m (Figure 1, Murphy et al., 2018)

2.0 Methods

2.1 Rainfall

We recorded rainfall, starting on January 27, 2016, along with temperature, atmospheric pressure, and relative humidity in 10-minute intervals using sensors manufactured by Onset corporation and stored using their Hobo Micro Station Data Logger. All weather station components were mounted <2 m above the ground surface on a stable hillslope adjacent to the

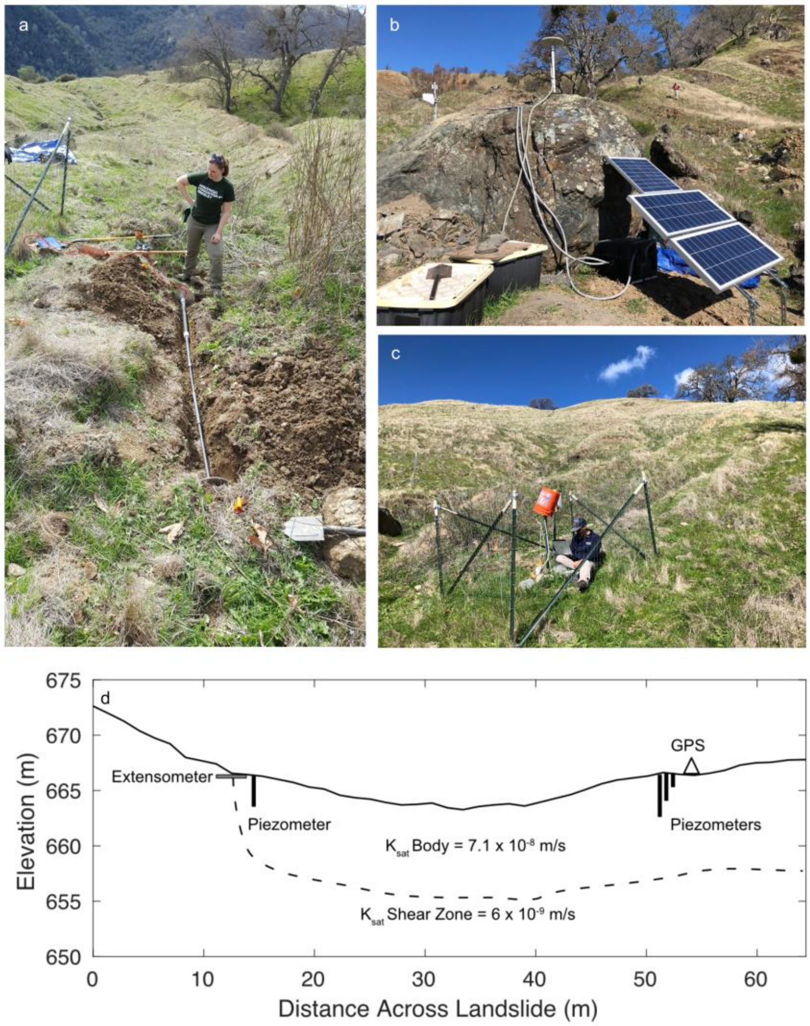

Figure 2. Field instrumentation: a) Vibrating wire extensometer being installed across lateral shear margin of landslide; b) Continuous GPS station (OREO); c) location of 2.7 m deep vibrating wire piezometer along lateral shear margin; d) Cross-section showing the locations and depths of instrumentation. The cross-section line corresponds to the yellow dashed line in Figure 1b. Dashed black line represents the inferred location of the landslide shear zone. Hydraulic conductivity (K_{sat}) values for slide body and shear zone correspond to those used for the variably saturated flow model.

earthflow (Figure 1a,b and Figure 2c). The rainfall sensor has a tipping bucket mechanism that summed rainfall in 2 mm increments over each 10-minute recording interval. For the period from January 1, 2015 to January 27, 2016, which we use to spin up our variably saturated flow modeling, we use rainfall data from the San Francisco Public Utilities Commission for Poverty Ridge, which is ~ 2 km from the earthflow monitoring site and is available via the California Department of Water Resources California Data Exchange Center (http://cdec.water.ca.gov/dynamicapp/staMeta?station_id=POV). We compared the two records where they overlap and found that after multiplying the Poverty Ridge Data by 1.1, we could reproduce within 1% the total cumulative rainfall observed at Oak Ridge between January 2016 and January 2020 (Figure S1). Hence, we combined the adjusted Poverty Ridge record with the measured Oak Ridge data to yield a continuous daily rainfall record starting on January 1, 2015.

2.2 Pore water pressure

We recorded pore water pressure in 10-minute intervals using vibrating-wire piezometers (RST Instruments, model VW2100-0.07) installed at two locations (Figure 1a,b). The first location is in the western lateral shear zone of the earthflow (Figure 2c), where a piezometer was installed to a depth of 2.7 m on February 5, 2016. This instrument operated continuously over the study period, with the exception of a hiatus from December 12, 2018 to April 4, 2019 due to a dead battery. The other location (Figure 1a,b) contains three piezometers installed at depths of 1.25, 2.5 and 4.2 m, respectively, within a few decimeters of one another at a location in the central portion of the earthflow body, approximately 50 m from the shear zone piezometer. The 2.5 m piezometer was installed on January 27, 2016 and operated continuously over the study period, with the exception of a hiatus from December 20, 2018 to March 15, 2019 due to a dead battery. The 4.2 m piezometer was installed on April 20, 2018 and the 1.25 m piezometer was installed on September 25, 2018. Both have recorded continuously since installation.

To install the piezometers, boreholes were manually excavated into mélange with a hand auger and backfilled with a grout slurry composed of water, cement, and bentonite (weight ratio = 2.49 : 1.00 : 0.41). This method is known as the 'fully-grouted' method of installation and is encouraged for vibrating wire piezometers (Contreras et al., 2007). An advantage of the fully grouted installation is that the vibrating wire piezometers can measure sub-atmospheric pressures under unsaturated conditions. Therefore, although the instruments cannot directly measure suction, they can be used to infer relative changes in suction head (down to ~-100 kPa) based on how far below atmospheric pressure the piezometer records (e.g., Mikkelsen & Green, 2003). Piezometers were attached to single-channel data loggers and programmed to record pressures at 10-minute intervals. The accuracy of the VW2100-0.07 at ≤ 70 kPa is 0.07 kPa with a precision of 0.0175 kPa. Piezometer readings were corrected for changes in ground temperature and atmospheric pressure using a linear calibration provided for each sensor by the manufacturer. Piezometer uncertainty (0.0175 kPa) was propagated into determinations of daily pore water pressure, as well as its rate of change.

Summer pore water pressure signals in some years are very far below atmospheric pressure (~ -20 kPa), and during other years are near zero throughout the summer or revert to zero abruptly in the midst of the summer. Because the ground surface is heavily fractured due to desiccation during the summer months, we assume that piezometers sometimes but not always equilibrate to atmospheric pressure during the summer depending on the details of the local fracture network. Hence, we interpret very negative pressures as the result of suction under conditions of low moisture content when the piezometer is far above the water table. For the reasons outlined above, we interpret pressure readings of near zero during the middle of the summer as an indication that the pore spaces around the piezometer are equilibrated to atmospheric pressure via the fracture network, not as saturation at the water table surface.

2.3 Earthflow displacement

To measure displacement of Oak Ridge earthflow, UNAVCO installed a Trimble NetR9 receiver and a Trimble GNSS Zephyr antenna bolted to a large boulder in the upper transport zone near the three piezometers (Figure 1b and Figure 2b). Data were telemetered to and processed by UNAVCO. Post-processing of GPS data was then conducted at the Nevada Geodetic Laboratory (Blewitt et al., 2018) and daily time series of positions were published online (http://geodesy.unr.edu/NGLStationPages/stations/OREO.sta). These positions were calculated in the NA12 terrestrial reference frame, which typically has a precision of 1.0 mm in the north, 0.9 mm east, and 3.4 mm in the vertical components (Blewitt et al., 2013). Daily, post-processed GPS positions were converted to daily displacements by subtracting background plate tectonic motion in the NA12 reference frame (~1.7 cm/yr towards the northwest), using data from two nearby permanent GPS stations installed on stable slopes (P253 and P227). Daily position uncertainties from the Nevada Geodetic Laboratory were analytically propagated into uncertainties in calculations of daily displacement. GPS-derived velocities were calculated over 11-day windows, which we found provides a good balance between temporal resolution, on the one hand, and uncertainty in velocity, on the other hand, which is larger for smaller time windows. To compute velocity uncertainty, we used a Monte Carlo approach in which we performed a linear fit to the displacement data over the 11-day window. We did this 100 times and in each iteration we added to the daily displacement measurements over the 11-day window a number drawn at random from a normal distribution whose standard deviation corresponds to the propagated uncertainty in displacement. We then assigned 11-day velocities and uncertainties based on the mean and standard deviation, respectively, of the Monte Carlo velocity determinations.

We also recorded earthflow displacement starting on January 15, 2018 using a vibrating-wire extensometer (RST Instruments, model EXSR-1300) that spanned the active earthflow margin, approximately two meters away from the shear zone piezometer (Figures 1a,b). The extensometer was buried to a depth of 20 cm and the long axis was oriented as close to parallel to the strike of the slickensided shear zone as possible, with the flanges located diagonally across from one another (Figure 2a). The lateral shear face became exposed in April 2017 when a >250 m-long (<5 cm wide) fissure opened along its length as the earthflow surface began to desiccate and crack (Nereson & Finnegan, 2019). Fresh roots of annual grasses along the shear surface were preferentially oriented in the direction of downslope movement, which indicated that this was the active shear zone in 2017. The extensometer was set to log data every 10 minutes, with a precision of 0.06 mm and an accuracy of 0.75 mm. Measurements were compensated for the geometry of the installation (the extensometer was oriented ~13° off strike of the shear plane) and for temperature variability using a linear calibration provided by the manufacturer to yield displacement in the downslope direction. Extensometer uncertainty (0.06 mm) was analytically propagated into determinations of daily displacement and daily velocity. The extensometer failed on April 3, 2019 when it extended beyond its 30 cm range.

2.4 Pore Fluid Pressure Diffusion Modeling

To test the predictions of the commonly used 1D pore pressure diffusion model that assumes full saturation, we solve equation (1) using the measured daily rainfall at Oak Ridge as the input for the 1D pore pressure diffusion model described in Handwerger et al. (2016; 2019). In addition to the precipitation at the surface, this model formulation requires measurements of hydraulic diffusivity and an infiltration scaling factor that is empirically calibrated. For the Oak Ridge record, we use a hydraulic diffusivity of 2×10^{-6} m^2/s, which does a good job of matching the seasonal frequency of the observed pore water pressure changes and agrees with values from other landslides in the Franciscan mélange (Iverson, 2000, 2005), and a scaling factor of 3000, which does a good job of matching its amplitude.

2.5 Variably Saturated Groundwater Modeling

To glean an understanding of how unsaturated zone flow modulates landslide response to precipitation, we use the composite rainfall record at Oak Ridge earthflow to forward-model a one-dimensional approximation of the landslide hydrology using the USGS software vs2dt (Healy, 1990; Lappala et al., 1987). vs2dt is a numerical model that uses a finite-difference approach to solve the head-based (ψ) formulation of the Richardson-Richards equation (Richards, 1931; Richardson, 1922), which in one dimension can be represented as:

$$\partial/_{\partial z}\left[K(\psi)\left(\partial\psi/_{\partial z}-1\right)\right]=c(\psi)\,\partial\psi/_{\partial t} \qquad (9)$$

where $c(\psi)$ is referred to as the specific moisture capacity and is equal to the gradient of water content, θ, with respect to capillary head, $\partial\theta/_{\partial\psi}$. Because both moisture content and hydraulic conductivity, K, vary with capillary head above the water table, solving this equation requires a constitutive relationship between K, θ, and ψ, often called a characteristic moisture curve. Here we use the relationships of van Genuchten (1980) and Mualem (1976) to parameterize the characteristic moisture curve for Oak Ridge Earthflow (Table S1).

Although vs2dt can solve problems in two dimensions, here we approximate the landslide hydrology with a 1d vertical column (e.g., Iverson, 2000) with a thickness of 7.5 m and a grid size of one cm to represent the main landslide body and a thin, 0.5 m thick basal shear zone (Fig. S6). We impose a vertical flux boundary condition at the top of the model domain using the composite rainfall record described in 2.1 and we impose a gravity drain boundary condition at the base of the slide. We do not model evapotranspiration because the invasive grasses that colonize the landslide, which have shallow roots to begin with, are largely dormant during the period when the landslide is active (Nereson et al., 2018). Our assumption of a gravity drain boundary condition is justified by the fact that the boundary of the landslide at the location of our instrumentation appears to be defined by a contact between low hydraulic conductivity mudstone and higher hydraulic conductivity sandstone, which results in a perched water table within the landslide body overlying a much deeper water table (Murphy et al., 2018). We note that Hahm et al. (2019) noted similar conductivity contrasts between Franciscan mudstone and sandstone blocks. We use an estimated saturated hydraulic conductivity value of 7.1 x 10^{-8} m/s for the landslide body (Murphy et al. 2018) and an inferred value of 6 x 10^{-9} m/s for the landslide base, where we lack direct measurements. These values are generally consistent, if a little lower, than near surface hydraulic conductivity measured elsewhere in Franciscan mélange (Dralle et al., 2018). Because of the gravity drain lower boundary condition, the flux out of the model at every time step is equal to the saturated hydraulic conductivity of the landslide base. Notably, without a basal hydraulic conductivity in the model that is lower than the conductivity of the landslide body, we are unable to sustain positive pore water pressures within the landslide body. That said, a lower basal hydraulic conductivity relative to the landslide body is an expected consequence of clay alignment and grain crushing within a landslide's basal shear zone (Baum & Reid, 2000; Wang et al., 2010).

Our modeling goal here is not to directly replicate the observed pore water pressure record, but instead to use the hydrologic modeling to understand the general processes of unsaturated flow that ultimately govern the timing of landslide displacement here. Accordingly, we adopt the simplest approach possible that will enable us to isolate the role of unsaturated flow dynamics in governing pore water pressure evolution. At the same time, we acknowledge that using a more detailed representation of preferential flow paths (Sidle & Bogaard, 2016), particularly fracture flow (Krzeminska et al., 2013; Shao et al., 2016), or material heterogeneity with depth (Malet et al., 2005) would likely enable us to fit the pore fluid pressure more exactly.

We chose to use the 2.5 m deep piezometer as our reference pressure record. For this piezometer, the pressure data show that the water table rarely rises above a depth of about 0.5 m below the ground surface, even under conditions of ponding water on the landslide surface. We suspect that the lack of local saturation to the landslide surface at the location of our piezometers results from hummocky earthflow topography that creates deviations above and below the mean landslide elevation and therefore prevents the water table from perfectly mimicking the topographic surface (Iverson and Major, 1987). In addition, slope-parallel channels on either side of the piezometer may induce lateral drainage that also prevents the water table from reaching the topographic surface at the location of our piezometer (Figure 1b). Because we cannot replicate these effects in a one-dimensional model, we make the simplification described above to the model domain. Again, our emphasis here is on capturing the general vadose zone processes at our site without simulating in detail the 2D and 3D effects that are likely required to capture the details of the piezometric response at our site.

3.0 Results

3.1 Rainfall

Rainfall, as is typical in California, occurs almost exclusively between the months of October and May, with individual storm events delivering as much as 60 mm of rain during a day (Figure 3a). Total water year (Oct 1 - Sept 30) rainfall measured at Oak Ridge was 666 mm in water year 2016, 845 mm in water year 2017, 520 mm in water year 2018, 743 mm in water year 2019, and 427 mm in water year 2020, which reflects an average annual precipitation depth of 640 mm during our study period. We also note that water year 2016 marked the end of one of the driest periods (2012-2016) ever recorded in the state of California (Lund et al., 2018). Water year 2017, in contrast, was the second wettest year recorded in the state of California (Singh et al., 2018)

3.2 Pore water Pressure

The early season rise of the water table above our piezometers is typically very abrupt (Figure 3b), but occurs weeks to months after the onset of seasonal rainfall (Figure 4). For example, in 2016 the onset of the rainy season was marked by 12 rainfall events in 60 days and 179 mm of rainfall during which pressures in the two shallow piezometers (2.5 and 2.7 m deep) were negative, indicating unsaturated conditions, and declining (Figure 3a,b). However, following the 13th rainfall event of that season (December 15, 2016), pore water pressures increased rapidly to positive values. On December 16, 2016, approximately 50% of the total pore water pressure change over the wet season occurred in one day, when the water pressure rose ~ 8 kPa (Figure 4), or an equivalent of ~ 0.8 m of head change. In each year of our record, the onset of saturation in our piezometers is accompanied by a rapid pressure rise, although not as dramatic as in 2016 (Figure 4). Once the water table rises above the level of our piezometers, the pore water pressure

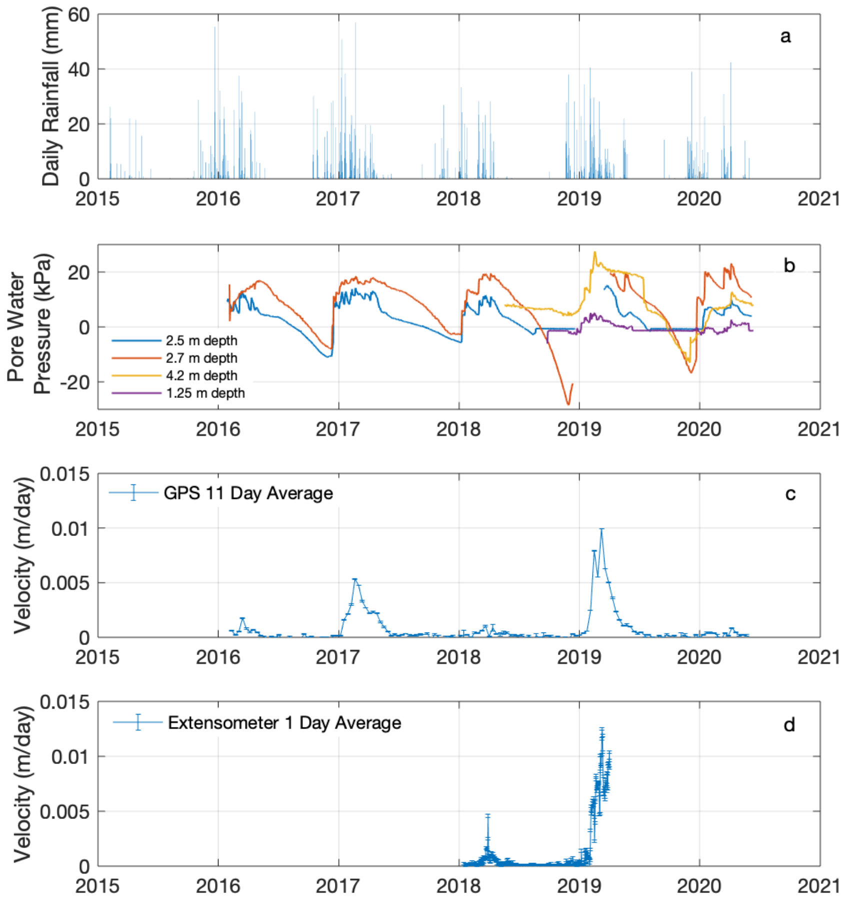

Figure 3. Time series monitoring data at Oak Ridge earthflow. a) Daily rainfall record from Oak Ridge earthflow for the study period. b) Pore fluid pressure record from the four piezometers shown in 1b for the study period. c) Velocity computed over an 11-day window from the GPS station shown in 2b. Error bars reflect the velocity uncertainty over the 11-day window, as described in section 2.3 d) Velocity computed over a 1-day window from the vibrating wire extensometer shown in 2a. Error bars reflect the velocity uncertainty over the 1-day window, as described in section 2.3

signal is characterized by much more temporal variability (Figure 4), with 1-2 kPa increases of pressure that occur in association with individual rainfall events before quickly dissipating. When the water table was near the ground surface, comparison of pressure records for our deepest and shallowest piezometers during the winter of 2018-2019 shows that pore water pressure transmission occurs essentially instantaneously in response to rainfall events, with no observable lag or attenuation with depth (Figure 5a-b).

3.3 Landslide Displacement

We never observe landslide motion prior to the water table rising above the level of our piezometers (Figure 3b-d), suggesting that the conditions when equation 1 is satisfied (i.e., Coulomb failure) occur only when the water table is close to the ground surface, as also observed

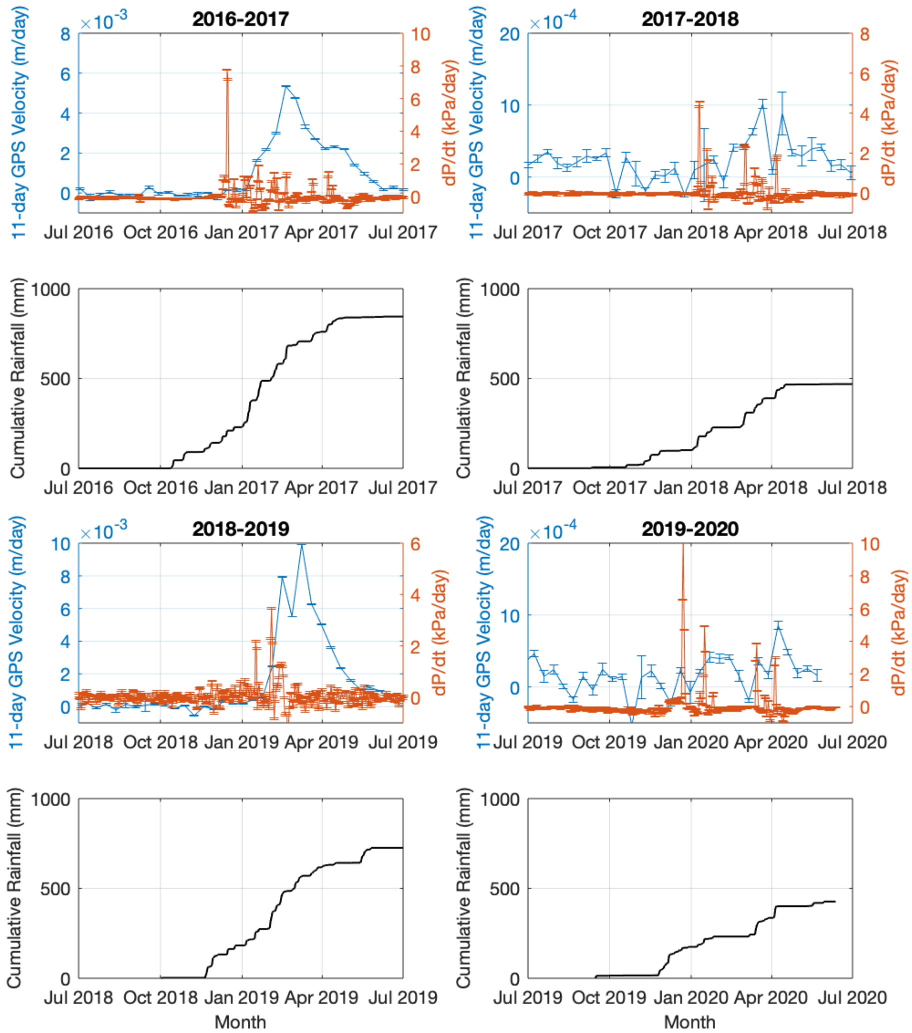

Figure 4. For the four complete winter rainfall seasons examined in this study, the top panel compares velocity, as measured by GPS (blue), and the time derivative of pore water pressure (orange). Error bars for velocity (blue) reflect the velocity uncertainty over the 11-day window, as described in section 2.3 Error bars on the derivative of pore pressure (orange) show the propagated piezometer precision, as described in section 2.2. The bottom panel shows cumulative rainfall over the same period (black). For 2016-2017 and 2017-2018, we use the pressure record from the 2.5 m piezometer; for 2018-2019, we use the 4.2 m piezometer; and, for 2019-2020, we use the 2.7 m piezometer.

at another slow landslide in the Franciscan mélange (Iverson and Major, 1987). For the four years examined here, the pore water pressure associated with landslide motion was exceeded when or shortly after the rapid rise in pressure described in section 3.2 (Figure 4). When pore water pressures were sustained at high levels in the landslide, as occurred in the winter of 2018-2019, we were able to clearly observe landslide acceleration measured by the extensometer due to pulses of pressure at depth triggered by individual rain events (Figure 6a-b). This observation, taken together with Figure 5, shows that once the landslide is near saturation, acceleration occurs

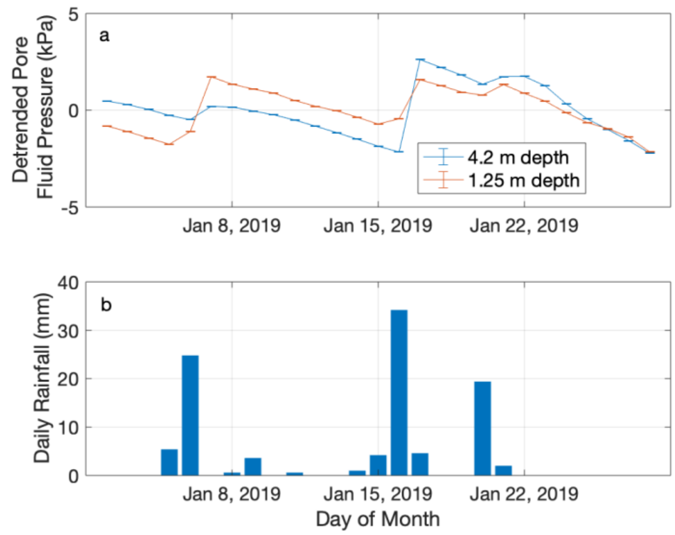

Figure 5. Comparison of pore water pressure measured at two depths. a) Detrended pore fluid pressure records from the deepest (4.2 m) and shallowest (1.25 m) piezometers during January, 2019. b) Daily rainfall during the same period. Uncertainties on pressure reflect the piezometer precision.

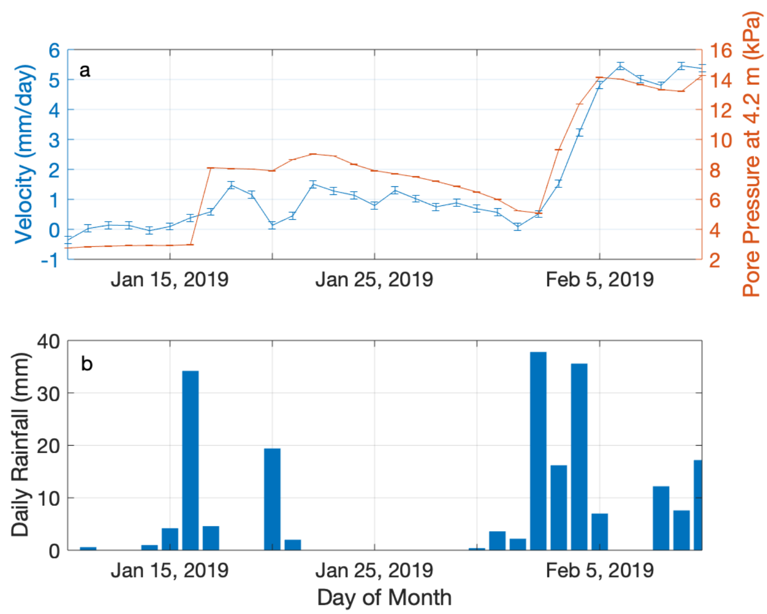

Figure 6. Velocity, pore pressure and rainfall measurements during winter 2019. a) Daily average pore fluid pressure from the 4.2 m piezometer compared to daily velocity from the extensometer during January and February 2019. Error bars for pressure (orange) reflect the piezometer precision. Error bars for velocity (blue) reflect the velocity uncertainty over the 11-day window, as described in section 2.3. b) Daily rainfall for the same period.

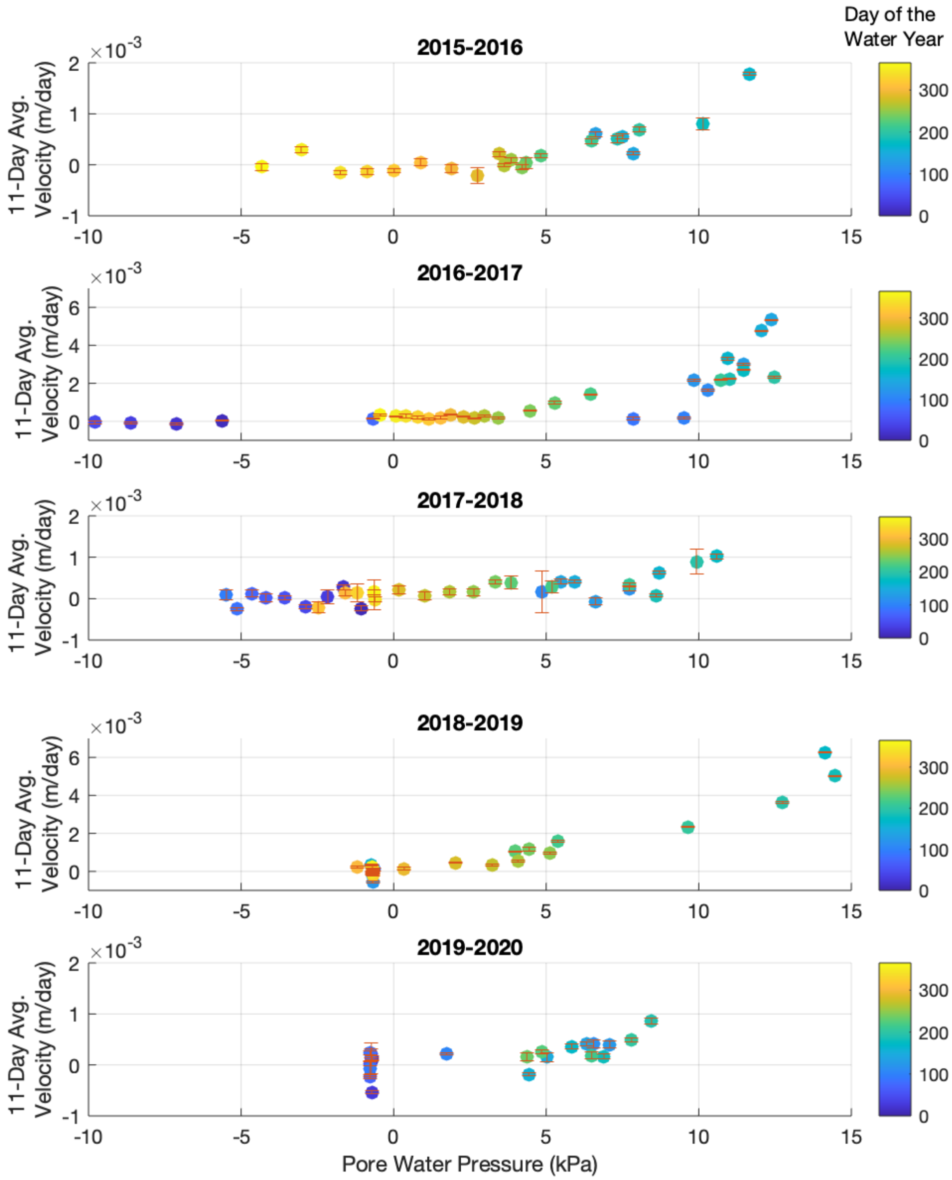

Figure 7. Plots of the 11-day average GPS-derived velocity for Oak Ridge Earthflow for each water year (Oct. 1 – Sept. 30) of the study compared to the median pore fluid pressure from the 2.5 m deep piezometer record for the same 11-day period over which velocity was computed. Note that in 2019-2020 the piezometer was offline during the seasonal rise of the water table and during the peak in pore pressure, so it only captures the falling limb of the seasonal water table cycle. In addition, during 2015-2016 we did not record the entire rise of the water table. Uncertainties in 11-day velocity, as described in the Methods, are shown with red error bars.

within ~ 1 day of rainfall events, implying a hydraulic diffusivity of ~ 10^{-4} m^2/s assuming an ~8 m deep failure surface (based on the characteristic diffusion time scale).

Figure 7 summarizes the annual relationship between pore water pressure, in this case measured by the 2.5 m deep piezometer, and landslide displacement rates. The figure shows a coherent relationship between pore water pressure and sliding velocity from year to year. The observed relationship between sliding velocity and pore fluid pressure also generally supports the existence of a pore pressure threshold that governs the onset of landslide motion (Figure 7, S2 and S3). Depending on the piezometer used and the year in question, we also observe up to a ~ 5 kPa difference in the pore water pressure marking the onset of motion and cessation of motion (Figure 7, 2016-2017). However, neither the magnitude nor sense of this hysteresis is consistent between our different piezometers (Figures S2, S3).

Figure 7 also demonstrates that landslide displacement rates are sensitive to small changes in pore water pressure, as also observed in other slow-moving landslides (Corominas et al., 2005; Malet et al., 2002; Schulz et al., 2009) as well as in experiments of landslide materials that are brought to failure by increasing pore water pressure (Agliardi et al., 2020; Carey et al., 2019). Indeed, the entire range of sliding velocities observed occur within a < 5 kPa range of pore water pressure variation.

3.3 Pore Pressure Diffusion Modeling

The 1D diffusion modeling captures the general seasonal rise and fall of the water table that is observed at Oak Ridge earthflow (Figure 8a,b). However, detailed comparison of the modeled pressure from assuming linear diffusion and the observed pore pressure shows that the diffusion model overestimates early season pore pressures (Figure 8b). For example during the winters of 2016-2017 and 2017-2018, the linear diffusion model predicts positive pressures of up to ~ 5 kPa at 2.5 m depth for many weeks when an unsaturated state (and therefore negative pore pressure) was actually observed. At the same time, when the water table was close to the surface, the linear diffusion model was unable to reproduce the observed high frequency pressure spikes that occur in association with individual rainfall events (Figure 8b). Hence, during these periods the model commonly predicts pore water pressures at 2.5 m depth that are up to ~ 5 kPa lower than observed pore water pressures.

3.4 Groundwater Modeling

The one-dimensional Richards equation modeling, in contrast, better captures the seasonal timing of the rising water table, as well as the magnitude of fluctuations of the 2.5 m depth piezometer (Figure 8b) due to the observed rainfall. For example, the model reproduces both the subdued initial peak and subsequent late-season water table rise in Water Year 2018 as well as the rapid early season water table rise in the fall of 2016 (Figure 9).

In general, the model results show that the abrupt annual rise of the water table during the rainy season is dictated by the arrival of a single seasonal infiltration front that integrates a number of rainfall events through the vadose zone (Figures 9-11). When the infiltration front meets the draining water table surface, the water table begins to rise at a rate that is dependent upon the flux of water through the vadose zone, which is large when conditions are near saturation and moisture storage is limited.

To examine the propagation of seasonal wetting fronts more closely, in Figure 10 we show bi-weekly plots of modeled subsurface saturation (S_e), where $S_e = (\theta - \theta_r)(\theta_s - \theta_r)^{-1}$, from

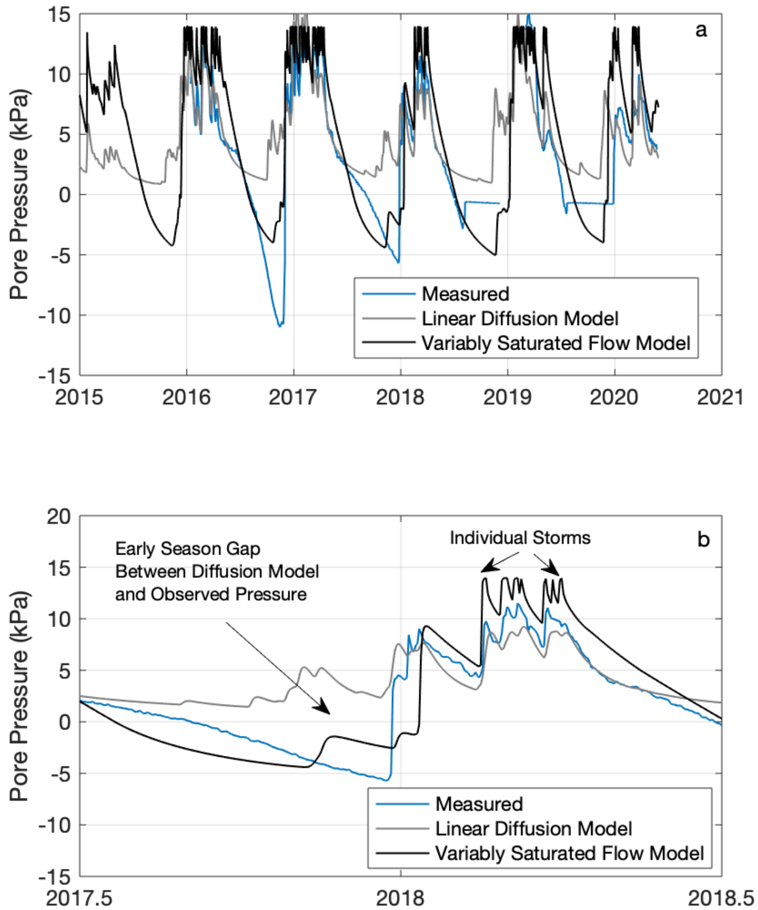

Figure 8. Modeled and measured pore water pressure for Oak Ridge earthflow. a) Comparison of measured pore water pressure at 2.5 m depth and modeled pore water pressure at 2.5 m depth from the 1D saturated linear diffusion model and from numerical solution of the Richards-Richardson equation. b.) Close-up of one year highlighting the differences between the different modeling approaches.

October 1st-February 1st for water years 2017-2020. Early rainy season moisture profiles reflect the groundwater capillary profile, and as storms begin to arrive wetting fronts can be seen propagating down from the surface as a high-saturation kink in the upper profile. For each water year we also show the calculated moisture pulsivity P from the arrival of the first storm, subjectively defined as the first daily rain to exceed 10 mm, to the first modeled piezometer exceedance of 10 kPa (e.g., Fig. 9b). We choose this time window as it best reflects the period over which significant infiltration occurs in the lead-up to motion onset.

Water year 2020 provides the most straightforward picture of modeled infiltration dynamics, where the relatively shallow water table depth at the beginning of the rainy season leads to high surface saturation values of ~0.9, and rapid rainfall beginning in late November 2019 results in a

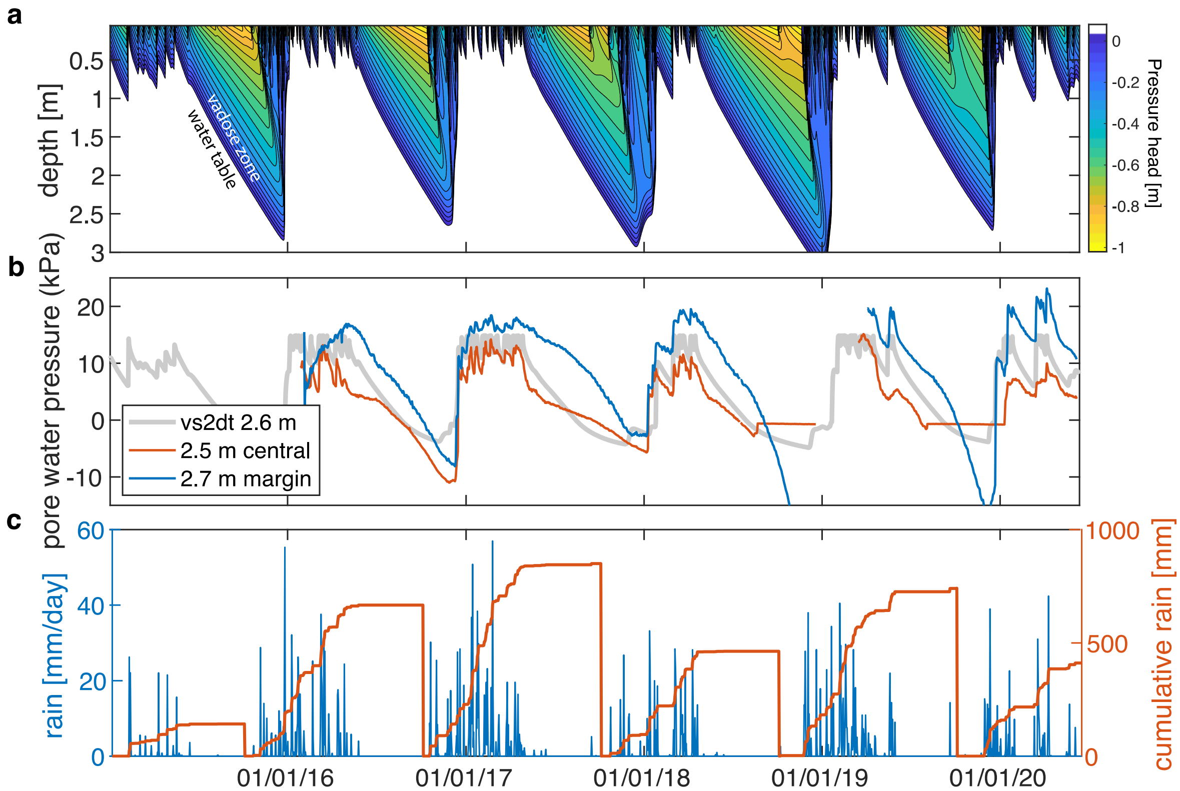

Figure 9. Modeled and measured pore water pressure for Oak Ridge earthflow. a) vs2dt model results shown in contours of tension pressure head (-5 cm contours). The white region indicates the water table depth, and filled contours therefore represent the depth of the vadose zone over time. b) Comparison of 2.5 m depth piezometer data (red line) and 2.7 m piezometer at the slide margin (blue) with modeled piezometer 2.6 m-equivalent results (grey). c) Rainfall record used as the input for the 1D model, shown as daily totals (blue, left axis) and seasonal cumulative totals (orange, right axis).

near-fully saturated wetting front that rapidly propagates to the water table (Fig. 10). Here the relatively high cadence of rainfall delivery after the first significant storm, and the limited fillable pore space controlled by the high initial water table position, lead to a low pulsivity value that is reflected in the uniform slug of water delivered to the water table. Water Year 2019 shows a similar time series of saturation profiles, although a dryer vadose zone controlled by the lower initial water table position (Fig. 9) results in a slower wetting front propagation (Fig. 10) and pore water pressure response. While the style of moisture delivery is similar, reflected in similar pulsivity values, the delayed water table response in WY2019 relative to WY2020 highlights the strong control nonlinear capillary moisture storage exerts on the downward propagation rate of infiltrating water and therefore the timing of initial seasonal porewater pressure rise.

Conversely, model results for Water Year 2018 show a more complicated picture of early season surface water delivery, with longer hiatuses between storms. The slower pace of rainfall results in a pulsivity value of >2, and the moisture profiles indeed show an initial wetting front propagation, followed by drying of the vadose zone and a second wetting front propagation that ultimately drives the water table to the surface (Fig. 10). The consequent pore water pressure

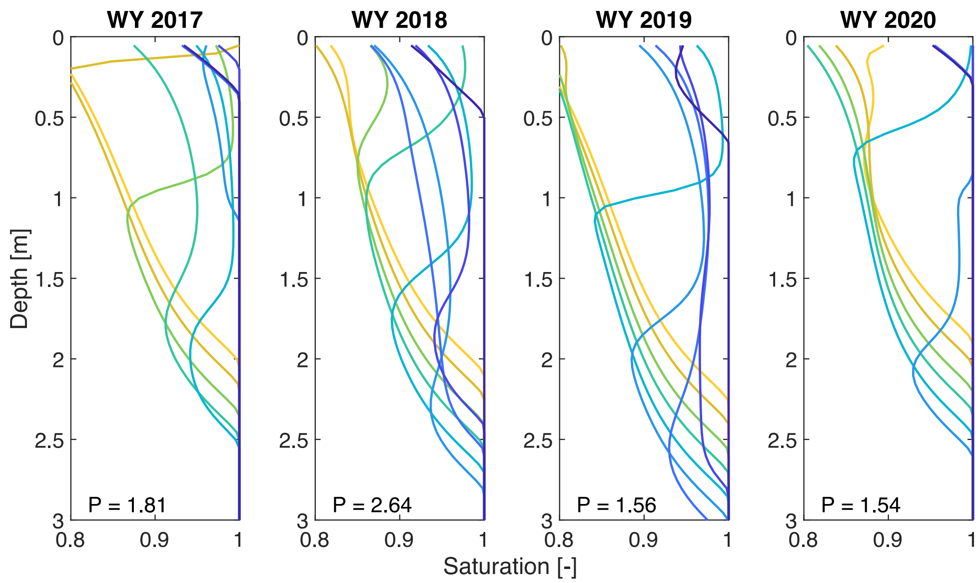

Figure 10. Bi-weekly profiles of subsurface saturation from October 1st (yellow) to February 1st (dark blue) for Water Years 2017-2020. Early season profiles show the moisture content set by the groundwater table, and kinks in the profiles show the downward propagation of wetting fronts. Moisture pulsivity (P) values calculated from the onset of the first storm to the exceedance of 10 kPa for the modeled piezometer data (Fig. 9b) are shown at the bottom-left of for each Water Year.

response reflects this in a series of defined pore water pressure peaks in the lead-up to landslide motion (Figs. 9 and 4).

In Figure 11, we show the storm surface connectivity C_s (equation 8) for WY 2019 alongside a time series of modeled pressure head above the water table in the upper 3 m of the landslide. Because the surface often fully saturates during a rainfall event, C_s is calculated by taking the average fillable porosity above the water table at each time step, and a conservative reference rainfall depth of 20 mm is used, which approximates a typical large storm that Oak Ridge experiences (Fig. 3a). As storms begin arriving in late November 2018 and water begins infiltrating from the landslide surface (white dashed line in Fig. 11a), vadose zone storage declines and C_s begins to increase. In mid-January, the leading edge of the seasonal wetting front connects to the water table, adding enough groundwater recharge to cause the water table to begin rising. At this point, full surface connectivity is reached and C_s goes from 0.8 to 1. The next storm then arrives, fully connecting to the water table and causing it (and hence the pore water pressure at depth) to rapidly rise. Connectivity then stays at a value of 1 through the winter and early spring, and individual storm events cause the landslide to accelerate, shown by increases in the slope of GPS cumulative displacement (Fig. 11b). As the rainy season subsides through Spring and Summer 2019, the reference connectivity remains at 1 until the water table is sufficiently low and vadose zone storage exceeds the reference rainfall depth. Here it is worth noting that while the late-Spring storm events drive the water table to the surface in the vs2dt Richards equation model, here the linear diffusion model better captures the relatively low magnitude of pore water pressure increase recorded by the piezometers (Fig. 8a).

4.0 Discussion

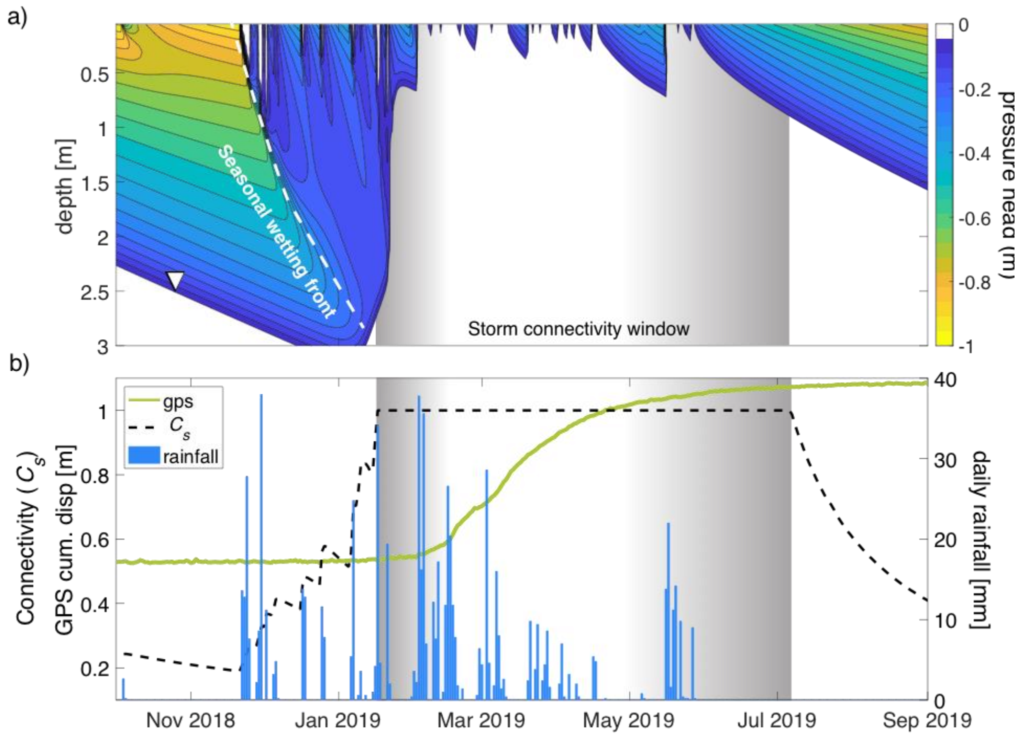

Figure 11. a) Zoomed in vs2dt model results for water year 2019 showing the infiltration of rainwater through the unsaturated zone and subsequent water table response (lowest contour is indicated with ∇ symbol). Bold white dashed line shows the general trajectory of the seasonal wetting front that originates at the beginning of the rainy season. Pressures heads ≥ 0 are shown in white, and pressure pulses associated with individual storms can be seen projecting down from the ground surface. Panel b) shows the daily rainfall on the right axis, and the cumulative GPS displacement (green) as well as the storm surface connectivity C_s (black dashed line). Cs is calculated using the average fillable pore space in the vadose zone at each time step in the model run, and a reference rainfall depth of 20 mm. When the connectivity reaches a value of one, that implies that entirety of infiltrating water from a reference storm will connect to the water table directly from the surface. Connectivity values stay elevated past the rainy season until the water table is sufficiently low and the vadose zone is sufficiently dry. Here Cs reaches 1 approximately one week before the next storm arrives and connects to the water table, driving up pore water pressures in the landslide and initiating motion.

Our objective in this paper is to exploit a well instrumented, slow-moving landslide that experiences seasonal unsaturated conditions to understand how the seasonal pore water pressure and deformation response of a large landslide to rainfall infiltration is modulated by infiltration of water through the vadose zone. Below we discuss the relationship between pore water pressure and deformation observed at Oak Ridge earthflow, and then the seasonal relationship between rainfall and pore pressure response both at Oak Ridge and more generally for landslides that are also controlled by vadose zone hydrology.

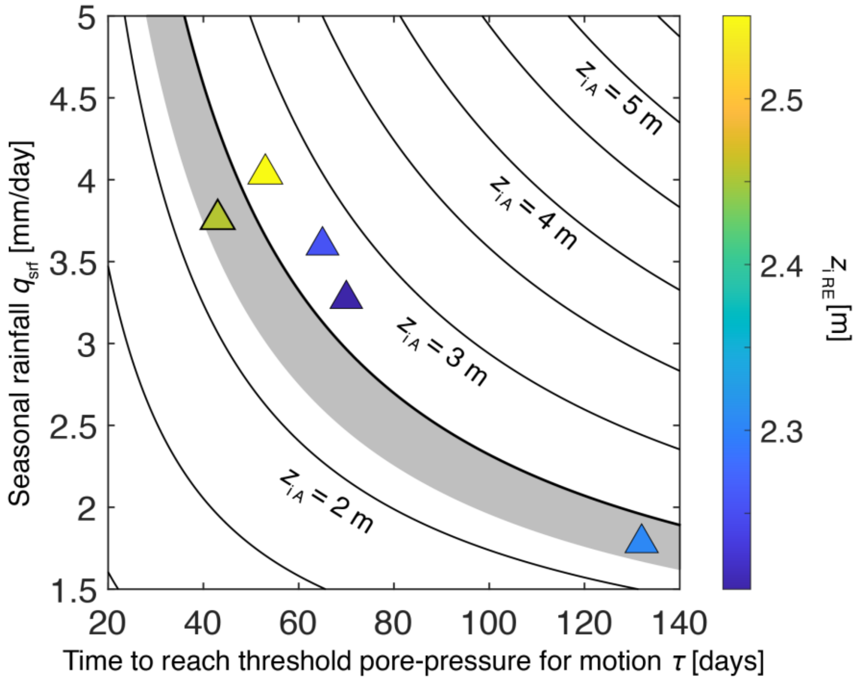

Figure 12. Rainfall and modeled water table data plotted with seasonal rainfall intensity (q_{srf}) - duration (T) thresholds for the onset of motion at Oak Ridge earthflow from equation (9) assuming initial water table elevations (z_i) at 2.2 and 2.5 m depth (gray envelope). z_{iRE} is color-coded to show the initial water table elevation at the beginning of rainfall in the Richardson/Richards equation model. T is calculated as time from the onset of seasonal rainfall to when the modeled landslide water table reaches a 10 kPa threshold (~0.5 m depth), and q_{srf} is calculated by dividing the total rainfall by T.

Our monitoring results show that at Oak Ridge earthflow landslide motion is strongly seasonal, ceasing from late summer to early winter, and only resuming again well after the first winter rains begin in the Fall (Figure 3b-d). The relationship between sliding velocity and pore water pressure revealed by our deformation monitoring (Figures 7, S2 and S3), as noted in 3.3, is consistent with observations at other slow-moving landslides that reveal a non-linear relationship between sliding velocity and pore water pressure (e.g., Malet et al., 2002). In addition, the data support the presence of a pore water pressure threshold that governs the seasonal onset of landslide motion, as expected from equation 1. However we note up to a ~ 5 kPa difference between the pore water pressure at the onset of motion compared to when motion ceases over a given wet season. Although this is still relatively modest hysteresis compared to observations in other landslides (van Asch, 2005; Massey et al., 2013) as well as experiments (Carey et al., 2019), we acknowledge that at Oak Ridge there may not be a simple mapping of pore fluid pressure variation onto velocity (e.g., Schulz et al., 2018), even if the seasonal onset of motion appears to be governed by an identifiable pressure threshold. That said, neither the amount nor sense of hysteresis is consistent between piezometers, suggesting that some caution should be used in interpreting the details of the relationship between pressure and velocity for a given piezometer. Hysteresis aside, we do observe a robust relationship of seasonal landslide acceleration during periods of rising pore fluid pressure and landslide deceleration during periods of dropping pore pressure (Figure S4). This observation is suggestive of an apparently quasi-stable relationship between sliding velocity and pore water pressure. However what the process is that governs this relationship and how we might use the data in Figures 7, S2 and S3 to test this remains beyond the aims of this paper.

Our numerical modeling suggests that the primary hydrologic dynamics that drive seasonal pore water pressure changes over time in the landslide body (Figure 9) can be captured only through consideration of vertical unsaturated flow with relatively few tunable parameters. Hence, these results are likely generalizable to many settings. We also recognize that a similar temporal evolution of the water table observed at Super-Sauze earthflow in the French Alps (Malet et al., 2005) is well described by a dual permeability model that explicitly models flow along fissures (Krzeminska et al., 2013). These more complex models may better describe complex landslide hydrology, but at Oak Ridge, our relatively simple model reproduces the salient features of the seasonal pore water pressure record with minimal parameterization.

In contrast, the more commonly used linear pore pressure diffusion model, which was explicitly intended only for use under saturated conditions (Reid, 1994; Iverson, 2000), systematically over predicts early season pore water pressures and systematically underpredicts pore water pressures as saturation is approached (Figure 8a). This is an expected consequence of assuming hydraulic conductivity (and hence hydraulic diffusivity) that is fixed throughout the year, instead of allowing it to evolve with moisture content. The ~ 5 kPa misfit between the diffusion model and the measured pore water pressures is significant because most of the annual velocity variation occurs due to changes in pore water pressure that are of a similar ~ 5 kPa magnitude (e.g., Figure 7). Consequently, for predicting the onset of seasonal slow landslide motion, there is premium on modeling the details of the pore water pressure evolution. For this application a variably saturated model does a better job of simulating the abrupt early season rise of the water table as well as its high frequency variability as saturation is approached (Figure 8b).

The key insight garnered from the 1D hydrological model results is that the rapid seasonal rise of the water table at Oak Ridge earthflow occurs only once the majority of the seasonal infiltration front, which marks the leading edge of the integrated downward flux of rainfall through the vadose zone, reaches the water table. After this point, rainfall is transmitted rapidly to the water table, instead of being stored within the vadose zone (e.g., Fig. 10c), and pore water pressures rise, leading to landslide acceleration once a pore water pressure threshold is crossed.

Furthermore, the soil moisture pulsivity (P) and storm surface connectivity (C_s) parameters, developed in Section 1 from consideration of simplified infiltration dynamics, reasonably describe the hydrologic dynamics when applied to the vs2dt model results. Years with lower seasonal rainfall rates and high initial fillable pore space, like WY2018, have higher pulsivities and show multiple pulses of wetting fronts and pore water pressure response (Fig. 10). P may therefore be a useful construct for differentiating and predicting the varying patterns of landslide hydrologic response. For the case of WY2019, we show that reference storm surface connectivity approaches 1 directly before a subsequent storm drives the rapid seasonal spike in pore water pressures. This suggests that estimates of C_s, perhaps with instrumental knowledge of material and soil moisture characteristics, might be a useful metric for forecasting pore water pressure transience in shallow unconfined aquifers like landslides.

In Section 3.4 we compare the timing of modeled landslide response for Water Years 2019 and 2020, which experience a similar early season rainfall forcing but start the rainy season with different water table elevations (Fig. 9). The faster wetting front propagation (Fig. 10) and initial pore water pressure rise in WY2020 illustrates the importance of antecedent moisture in governing the filling time and downward propagation rate of wetting fronts (e.g., Equation 4). Below we attempt to incorporate the variable moisture storage effect in a simplified mass balance framework to develop a rainfall intensity-duration (ID) equation for predicting the onset of seasonal landslide motion. We then use this equation to interpret the timing of the onset of landslide motion revealed by the field data and modeling results.

The water table (and hence pore water pressure) rise should reflect, in 1D, a mass-balance between the flux of rainfall into the slide and the flux of water out due to drainage through the bottom of the landslide, with seasonal growth of the water table occurring as the former flux exceeds the latter (e.g., Bogaard & Greco, 2016). In the event of slow rainfall delivery, comparatively more rainfall is required to raise the water table than if the same rainfall is delivered more rapidly. This is because shallow groundwater is always draining. At Oak Ridge earthflow, the rate of decline of pore water pressure is 1-2 kPa or 10-20 cm of pressure head per month during the summer when there is no recharge from rainfall (Figure 3b).

In shallow, unconfined aquifers, the volume of water released per unit decline in water table head, per unit cross sectional area, is called the apparent specific yield, S_{ya}. This quantity reflects the volume of fillable pore space above the water table (Freeze & Cherry, 1979), which is controlled by grain size and porosity distribution. For a volume of recharge R added to the water table, the water table will rise proportionally to the apparent specific yield:

$$R = \Delta h S_{ya} \tag{10}$$

where Δh is equal to the change in water table height. In the vadose zone, capillary water storage increases from the ground surface toward the water table, which results in a nonlinear depth dependence of S_{ya} that varies greatly between material types. For example, silt and clay-rich materials often hold much more water in tension above the water table, resulting in a larger capillary fringe (smaller S_{ya}) and hence large swings in water table height for a given volume of recharge added to the system. Crosbie et al. (2005) define S_{ya} for a change in water table elevation based on the Mualem (1976) and van Genuchten (1980) capillarity model:

$$S_{ya} = S_{yu} - \left[\frac{S_{yu}}{\left(1+\left(\alpha\left(\frac{z_i+z_f}{2}\right)\right)^{n}\right)^{1-\frac{1}{n}}}\right], \tag{11}$$

where z_i and z_f are the initial and final positions of the water table, n and α are material specific parameters, and S_{yu} corresponds to the ultimate specific yield, defined as the saturated volumetric moisture content θ_s (equal to material porosity) minus the residual moisture content θ_r (Freeze and Cherry, 1979). Residual moisture is defined as the remaining moisture content at infinitely high suction. The mass balance of equation (5) can be recast to include the effects of a draining water table (Crosbie et al., 2005):

$$R = \left(\Delta h_r + \dot{D}_R \Delta t\right) S_{ya} \tag{12}$$

where Δh_r is the change in water table height from recharge, and $\dot{D}_R$ is the water table lowering rate in the absence of recharge (Crosbie et al., 2005), which again is roughly 10-20 cm per month at Oak Ridge earthflow (Figure 3b). Equating R with the seasonal rainfall flux q_{srf} multiplied by the duration of rainfall (Δt) allows us to solve for the seasonal landslide response time scale, T_s, that is required to grow the water table to a specific depth, Δh_r

$$T_s = \Delta t = \frac{\Delta h_r S_{ya}}{q_{srf} - \dot{D}_R S_{ya}} \quad (13)$$

If a threshold water table height Δh_r can be estimated for Coulomb failure, as appears to be the case at Oak Ridge earthflow (Figures 7, S2, and S3) and other slow landslides (e.g., Iverson and Major, 1987), then equation (11) can serve as a physically based rainfall intensity-duration threshold for slow-moving landslide failure. This approach is akin to the "leaky barrel" approach by Wilson & Wieczorek (1995), but here we incorporate the effect of material capillarity on transient moisture storage. We use a ~10 kPa threshold for the onset of motion for the 2.5 m piezometer (Figure 7), equivalent to a water table depth of 0.5 m below the top of the model domain, as our upper bound for Δh_r. We then plot the expected rainfall intensity-duration curves required to reach the 10 kPa threshold starting from initial water table depths between 2.2 and 2.5 m, which reflect the range of modeled water table depths at the onset of rainfall for each season (Figure 12). We use our vs2dt model results, together with rainfall observations, to plot the estimated response timescale and average rainfall flux for each water year at Oak Ridge earthflow. For each year of the record, the combination of rainfall flux and response timescale falls near or above the threshold prediction from equation (13). This suggests that the timescale (T_s) required to elevate the water table within the vadose zone to a specific threshold height provides a physically-based means of predicting the timing of the onset of landslide motion based on available rainfall data and knowledge of cursory material and hydraulic properties.

Equation (13) does not consider the storage time of infiltrating water before it reaches the water table and therefore cannot be used to determine the style of water delivery. Because of this, it is best suited to landslides where the vadose zone transit time for a wetting front to reach the water table is short relative to the total recharge accumulation time, T_s. That said, our new intensity-duration timescale has clear advantages over the more commonly used characteristic pore water pressure diffusion timescale (e.g., Coe, 2012; Handwerger et al., 2013), which implies that each landslide should have a single timescalee to describe its response to rainfall, which directly contradicts our monitoring data.

Comparisons between seasonally deforming landslides within mélange along the US west coast reveal that the style of moisture delivery may be important for dictating seasonal motion. A coarse estimate of the early season pulsivity at Oak Ridge earthflow can be derived from estimates of the annual average Fall rainfall fluxes, (PRISM Climate Group, 2017; viewable at https://swclimatehub.info/data/county-temp-precip-maps/precipitation) and a saturated hydraulic conductivity of 7.1×10^{-8} m/s. From these data, and assuming a seven month rainy season and a θ_i value of 0.2, the mean annual Oak Ridge pulsivity is approximately 1.2. The Hooskanaden landslide in coastal southern Oregon is another deep landslide in a mélange-type rock unit, but has higher proportions of sandstone and siltstone units that have a much higher inferred effective hydraulic conductivity of 6.6×10^{-6} m/s (Xu et al., 2020). Even with a higher mean annual rainfall during the fall and winter months, the estimated mean annual pulsivity is ~17, an order of magnitude higher than at the Oak Ridge earthflow. This suggests that early season pore-pressure response might be strongly dictated by vadose zone material differences, and indeed, recent geodetic measurements show that motion of the Hooskanaden slide responds strongly to individual storm events during the early rainy season (Xu et al., 2020), which stands in contrast to Oak Ridge earthflow where multiple rainfall events can be integrated into large pressure spikes.

A consequence of the low pulsivity of the Oak Ridge earthflow is that because the slide effectively fully saturates near the threshold pore pressure for motion, there is limited dynamic range for increasingly large pore water pressure generation from rainfall alone that could lead the earthflow to fail catastrophically or surge. However, the non-linear relationship between pore pressure and velocity suggests that additional pore pressure rise from landslide deformation (for example due to compression) may lead to rapid motions (Agliardi et al., 2020; Booth et al., 2018; Iverson et al., 2000; Iverson, 2005). Deeper bedrock slides with deeper water tables and high unsaturated pulsivity may therefore experience a greater range of slide motion, and this is also observed from the geodetic record of the Hooskanaden slide (Xu et al., 2020). Hence, the critical zone processes that ultimately determine the depth of the vadose zone (e.g., Rempe & Dietrich, 2014) appear to exert a strong control on the dynamics of landslides. As noted above, one of the unique aspects of the Franciscan mélange is that it has a thin (< 3 m) seasonal vadose zone (Hahm et al., 2019; Iverson & Major, 1987; Schulz et al., 2018; Figure 9b), which likely arises within the framework of Rempe and Dietrich (2014) from low saturated hydraulic conductivity that inhibits lateral drainage and summer drawdown of the water table (Hahm et al., 2019). Thus, in the Franciscan mélange, pore water pressures are generally high at depth because the water table is always near the surface. This means that for a given gradient, hillslopes developed in mélange are always closer to Coulomb failure than in a setting with a deeper vadose zone where the water lowers more significantly during the summer (e.g., Hahm et al., 2019). This fact may explain the high density of currently active landslides in the Franciscan mélange (e.g., Mackey & Roering, 2011), the "melting ice cream" quality to the topography of the Franciscan mélange (Kelsey, 1978), as well the sensitivity of landslides in Franciscan mélange to base-level forcing (Bennett et al., 2016a) and year to year changes in rainfall (Bennett et al., 2016b; Handwerger et al., 2019). Because landscapes underlain by Franciscan mélange exist so close to the threshold for slow landslide failure, they are also likely to be acutely sensitive to future changes in precipitation in California, which will likely be characterized by increasing variability (Swain et al., 2018; Berg and Hall, 2015).

5.0 Conclusions

Linking temporal patterns of precipitation and landslide failure remains a basic goal of geomorphology and natural hazards research. In this contribution, we outline theoretically how vadose zone processes can control the style and timing of the piezometric response of slow landslides to seasonal rainfall. Whereas a slow-moving bedrock landslide with a high bulk hydraulic conductivity can quickly transmit individual rainfall pulses down to the water table, a landslide with lower hydraulic conductivity relative to the seasonal rainfall flux tends to integrate many storm events into a single pulse that quickly drives up pore water pressures upon meeting the water table weeks to months after seasonal rainfall has commenced. To test our theoretical expectations of the role of vadose zone processes in governing the onset of seasonal landslide motion, we combine variably saturated groundwater flow modeling with five years of monitoring at a well-instrumented, slow-moving landslide, Oak Ridge earthflow, that experiences seasonal unsaturated conditions. The onset of landslide motion at Oak Ridge earthflow occurs only after an abrupt rise in the water table to elevations near the landslide surface 52-129 days after winter rainfall commences. Model results confirm theoretical expectations and suggest that this abrupt rise in the water table occurs as the wetting front, which marks the leading edge of the integrated downward flux of seasonal rainfall, reaches the water table. We show that this non-linear response of the water table is an expected consequence of rainfall infiltration into unsaturated ground with the material properties observed at Oak Ridge. Prior to this abrupt rise, we see little measured pore water pressure response within the landslide due to rainfall. However, once the wetting front reaches the water table, we observe nearly instantaneous pore water pressure transmission to within the landslide body that is accompanied by landslide acceleration. We cast the timescale to reach a critical pore water pressure threshold using a simple mass balance model that considers unsaturated moisture storage with depth and explains the onset of seasonal landslide motion with a rainfall intensity-duration threshold. Our analysis shows that the combination of landslide hydraulic properties and vadose zone thickness, together, exert a strong but predictable control on both the style and timing of piezometric response to seasonal rainfall.

Acknowledgements

We thank Thom Bogaard, Bill Schulz, and two anonymous reviewers for their constructive comments that helped clarify and contextualize this manuscript. Funding for this work was provided through the Geomorphology and Land-use Dynamics Program of the National Science Foundation (EAR # 1658800 & EAR #1613122 to NJF) as well as a National Science Foundation Graduate Fellowship to ALN. Funding for JPP was provided by the USGS Geology, Minerals, Energy, & Geophysics Science Center. Part of this research was carried out at the Jet Propulsion Laboratory, California Institute of Technology, under a contract with the National Aeronautics and Space Administration (80NM0018D0004). We thank UNAVCO for support with GPS installation and the San Francisco Public Utility Commission and Russ Fields for granting access to the field site. In addition, we are grateful to the numerous undergraduate and graduate student field volunteers who assisted in aspects of the work presented here.

Data: GPS data used in this paper are archived by UNAVCO (https://www.unavco.org/instrumentation/networks/status/nota/overview/OREO) and post-processed GPS data are archived at University of Nevada Reno Geodesy Laboratory (http://geodesy.unr.edu/NGLStationPages/stations/OREO.sta). Extensometer, Pore water Pressure and Meteorological Data are archived by Hydroshare on the Oak Ridge Earthflow Observatory Data page (https://www.hydroshare.org/resource/8e024d2aeb22489c92dbf0c2a1db4608/)

References

Agliardi, F., Scuderi, M. M., Fusi, N., & Collettini, C. (2020). Slow-to-fast transition of giant creeping rockslides modulated by undrained loading in basal shear zones. *Nature Communications*, *11*(1), 1–11. https://doi.org/10.1038/s41467-020-15093-3

Alberti, S., Senogles, A., Kingen, K., Booth, A., Castro, P., DeKoekkoek, J., et al. (2020). The Hooskanaden Landslide: historic and recent surge behavior of an active earthflow on the Oregon Coast. *Landslides*. https://doi.org/10.1007/s10346-020-01466-8

Angeli, M. G., Gasparetto, P., Menotti, R. M., Pasuto, A., & Silvano, S. (1996). A visco-plastic model for slope analysis applied to a mudslide in Cortina d'Ampezzo, Italy. *Quarterly Journal of Engineering Geology and Hydrogeology*, *29*(3), 233-240.

van Asch, T. W. J. (2005). Modelling the hysteresis in the velocity pattern of slow-moving earth flows: the role of excess pore pressure. *Earth Surface Processes and Landforms*, *30*(4), 403–411. https://doi.org/10.1002/esp.1147

van Asch, T. W. J., Van Beek, L. P. H., & Bogaard, T. A. (2007). Problems in predicting the mobility of slow-moving landslides. *Engineering Geology*, *91*(1), 46–55. https://doi.org/10.1016/j.enggeo.2006.12.012

Baum, R. L., & Johnson, A. M. (1993). Steady movement of landslides in fine-grained soils: a model for sliding over an irregular slip surface. *Landslide Processes in Utah Observation and Theory*. Retrieved from http://agris.fao.org/agris-search/search.do?recordID=US9422776

Baum, R. L., & Reid, M. E. (1992). *Geology, hydrology and mechanics of the Alani-Paty Landslide, Manoa Valley, Oahu, Hawaii* (No. 92–501). *Open-File Report*. U.S. Geological Survey,. https://doi.org/10.3133/ofr92501

Baum, R. L., & Reid, M. E. (2000). Ground Water Isolation by Low-Permeability Clays in Landslide Shear Zones. In *Landslides in Research, Theory and Practice* (Vols. 1–0, p. 1: 139-144). Thomas Telford Publishing. https://doi.org/10.1680/lirtapv1.34617.0023

Baum, R. L., Savage, W. Z., & Godt, J. W. (2008). *TRIGRS - A Fortran Program for Transient Rainfall Infiltration and Grid-Based Regional Slope-Stability Analysis, Version 2.0* (Report No. 2008–1159). U.S. Geological Survey.

Bennett, G. L., Miller, S. R., Roering, J. J., & Schmidt, D. A. (2016a). Landslides, threshold slopes, and the survival of relict terrain in the wake of the Mendocino Triple Junction. *Geology*, *44*(5), 363–366. https://doi.org/10.1130/G37530.1

Bennett, G. L., Roering, J. J., Mackey, B. H., Handwerger, A. L., Schmidt, D. A., & Guillod, B. P. (2016b). Historic drought puts the brakes on earthflows in Northern California: Drought Puts Breaks on Earthflows. *Geophysical Research Letters*, *43*(11), 5725–5731. https://doi.org/10.1002/2016GL068378

Berg, N., & Hall, A. (2015). Increased interannual precipitation extremes over California under climate change. *Journal of Climate*, *28*(16), 6324-6334.

Berti, M., & Simoni, A. (2010). Field evidence of pore pressure diffusion in clayey soils prone to landsliding. *Journal of Geophysical Research: Earth Surface*, *115*(F3). https://doi.org/10.1029/2009JF001463

Berti, M., & Simoni, A. (2012). Observation and analysis of near-surface pore-pressure measurements in clay-shales slopes. *Hydrological Processes*, *26*(14), 2187–2205. https://doi.org/10.1002/hyp.7981

Blewitt, G., Kreemer, C., Hammond, W. C., & Goldfarb, J. M. (2013). Terrestrial reference frame NA12 for crustal deformation studies in North America. *Journal of Geodynamics*, *72*, 11–24. https://doi.org/10.1016/j.jog.2013.08.004

Blewitt, G., Hammond, W. C., & Kreemer, C. (2018). Harnessing the GPS Data Explosion for Interdisciplinary Science. https://doi.org/10.1029/2018eo104623

Bogaard, T. A., & van Asch, T. W. J. (2002). The role of the soil moisture balance in the unsaturated zone on movement and stability of the Beline landslide, France. *Earth Surface Processes and Landforms*, *27*(11), 1177–1188. https://doi.org/10.1002/esp.419

Bogaard, T. A., & Greco, R. (2016). Landslide hydrology: from hydrology to pore pressure. *WIREs Water*, *3*(3), 439–459. https://doi.org/10.1002/wat2.1126

Booth, A. M., McCarley, J., Hinkle, J., Shaw, S., Ampuero, J. P., & Lamb, M. P. (2018).

Transient reactivation of a deep-seated landslide by undrained loading captured with repeat airborne and terrestrial lidar. *Geophysical Research Letters*, *45*(10), 4841-4850.

Bouwer, H. (1978). *Groundwater hydrology*. New York: McGraw Hill.

Carey, J. M., Moore, R., & Petley, D. N. (2015). Patterns of movement in the Ventnor landslide complex, Isle of Wight, southern England. *Landslides*, *12*(6), 1107–1118. https://doi.org/10.1007/s10346-014-0538-1

Carey, J. M., Massey, C. I., Lyndsell, B., & Petley, D. N. (2019). Displacement mechanisms of slow-moving landslides in response to changes in porewater pressure and dynamic stress. *Earth Surface Dynamics*, *7*(3), 707–722.

Carrière, S. R., Jongmans, D., Chambon, G., Bièvre, G., Lanson, B., Bertello, L., et al. (2018). Rheological properties of clayey soils originating from flow-like landslides. *Landslides*, *15*(8), 1615–1630. https://doi.org/10.1007/s10346-018-0972-6

Coe, J. A, Ellis, W. L., Godt, J. W., Savage, W. Z., Savage, J. E., Michael, J. A., et al. (2003). Seasonal movement of the Slumgullion landslide determined from Global Positioning System surveys and field instrumentation, July 1998–March 2002. *Engineering Geology*, *68*(1), 67–101. https://doi.org/10.1016/S0013-7952(02)00199-0

Coe, Jeffrey A. (2012). Regional moisture balance control of landslide motion: Implications for landslide forecasting in a changing climate. *Geology*, *40*(4), 323–326. https://doi.org/10.1130/G32897.1

Cohen-Waeber, J., Bürgmann, R., Chaussard, E., Giannico, C., & Ferretti, A. (2018). Spatiotemporal Patterns of Precipitation-Modulated Landslide Deformation From Independent Component Analysis of InSAR Time Series. *Geophysical Research Letters*, *45*(4), 1878–1887. https://doi.org/10.1002/2017GL075950

Collins, B. D., Stock, J., Weber, L. C., Whitman, K., & Knepprath, N. (2012). Monitoring subsurface hydrologic response for precipitation-induced shallow landsliding in the San Francisco Bay area, California, USA. In *11th International Symposium on Landslides* (pp. 1249-1255).

Contreras Iván A., Grosser Aaron T., & Ver Strate Richard H. (n.d.). The Use of the Fully-Grouted Method for Piezometer Installation. *FMGM 2007*, 1–20. https://doi.org/10.1061/40940(307)67

Corominas, J., Moya, J., Ledesma, A., Lloret, A., & Gili, J. A. (2005). Prediction of ground displacements and velocities from groundwater level changes at the Vallcebre landslide (Eastern Pyrenees, Spain). *Landslides*, *2*(2), 83–96. https://doi.org/10.1007/s10346-005-0049-1

Crosbie, R. S., Binning, P., & Kalma, J. D. (2005). A time series approach to inferring groundwater recharge using the water table fluctuation method. *Water Resources Research*, *41*(1). https://doi.org/10.1029/2004WR003077

Dralle, D. N., Hahm, W. J., Rempe, D. M., Karst, N. J., Thompson, S. E., & Dietrich, W. E. (2018). Quantification of the seasonal hillslope water storage that does not drive streamflow. *Hydrological processes*, *32*(13), 1978-1992.

Freeze, R. A., & Cherry, J. A. (1979). *Groundwater* (1 edition). Englewood Cliffs, N.J: Prentice Hall.

Genuchten, M. T. van. (1980). A Closed-form Equation for Predicting the Hydraulic Conductivity of Unsaturated Soils. *Soil Science Society of America Journal*, *44*(5), 892–898. https://doi.org/10.2136/sssaj1980.03615995004400050002x

Gillham, R. W. (1984). The capillary fringe and its effect on water-table response. *Journal of Hydrology*, *67*(1), 307–324. https://doi.org/10.1016/0022-1694(84)90248-8

Hahm, W. J., Rempe, D. M., Dralle, D. N., Dawson, T. E., Lovill, S. M., Bryk, A. B., et al. (2019). Lithologically Controlled Subsurface Critical Zone Thickness and Water Storage Capacity Determine Regional Plant Community Composition. *Water Resources Research*, *55*(4), 3028–3055. https://doi.org/10.1029/2018WR023760

Handwerger, A. L., Roering, J. J., & Schmidt, D. A. (2013). Controls on the seasonal deformation of slow-moving landslides. *Earth and Planetary Science Letters*, *377–378*, 239–247. https://doi.org/10.1016/j.epsl.2013.06.047

Handwerger, A. L., Rempel, A. W., Skarbek, R. M., Roering, J. J., & Hilley, G. E. (2016). Rate-weakening friction characterizes both slow sliding and catastrophic failure of landslides. *Proceedings of the National Academy of Sciences*, *113*(37), 10281–10286. https://doi.org/10.1073/pnas.1607009113

Handwerger, A. L., Huang, M.-H., Fielding, E. J., Booth, A. M., & Bürgmann, R. (2019). A shift from drought to extreme rainfall drives a stable landslide to catastrophic failure. *Scientific Reports*, *9*(1), 1569. https://doi.org/10.1038/s41598-018-38300-0

Healy, R. W. (1990). *Simulation of Solute Transport Invariably Saturated Porous Media with Supplemental Information on Modifications to the U.S. Geological Survey's Computer Program VS2D*. Department of the Interior, U.S. Geological Survey.

Hu, X., Bürgmann, R., Lu, Z., Handwerger, A. L., Wang, T., & Miao, R. (2019). Mobility, Thickness, and Hydraulic Diffusivity of the Slow-Moving Monroe Landslide in California Revealed by L-Band Satellite Radar Interferometry. *Journal of Geophysical Research: Solid Earth*, *124*(7), 7504–7518. https://doi.org/10.1029/2019JB017560

Hu, X., Bürgmann, R., Schulz, W. H., & Fielding, E. J. (2020). Four-dimensional surface motions of the Slumgullion landslide and quantification of hydrometeorological forcing. *Nature Communications*, *11*(1), 1–9. https://doi.org/10.1038/s41467-020-16617-7

Hungr, O., Leroueil, S., & Picarelli, L. (2014). The Varnes classification of landslide types, an update. *Landslides*, *11*(2), 167–194. https://doi.org/10.1007/s10346-013-0436-y

Iverson, R. M. (2000). Landslide triggering by rain infiltration. *Water Resources Research*, *36*(7), 1897–1910. https://doi.org/10.1029/2000WR900090

Iverson, R. M. (2005). Regulation of landslide motion by dilatancy and pore pressure feedback. *Journal of Geophysical Research: Earth Surface*, *110*(F2). https://doi.org/10.1029/2004JF000268

Iverson, R. M., & Major, J. J. (1987). Rainfall, ground-water flow, and seasonal movement at Minor Creek landslide, northwestern California: Physical interpretation of empirical relations. *GSA Bulletin*, *99*(4), 579–594. https://doi.org/10.1130/0016-7606(1987)99<579:RGFASM>2.0.CO;2

Jibson, R. W. (2007). Regression models for estimating coseismic landslide displacement. *Engineering Geology*, *91*(2), 209–218. https://doi.org/10.1016/j.enggeo.2007.01.013

Keefer, D. K., & Johnson, A. M. (1983). *Earth flows; morphology, mobilization, and movement* (USGS Numbered Series No. 1264). U.S. G.P.O.,. Retrieved from http://pubs.er.usgs.gov/publication/pp1264

Kelsey, H. M. (1978). Earthflows in Franciscan melange, Van Duzen River basin, California. *Geology*, *6*(6), 361–364. https://doi.org/10.1130/0091-7613(1978)6<361:EIFMVD>2.0.CO;2

Krzeminska, D. M., Bogaard, T. A., Malet, J.-P., & van Beek, L. P. H. (2013). A model of hydrological and mechanical feedbacks of preferential fissure flow in a slow-moving landslide. *Hydrology and Earth System Sciences*, *17*(3), 947–959. https://doi.org/10.5194/hess-17-947-2013

Lacroix, P., Handwerger, A. L., & Bièvre, G. (2020). Life and death of slow-moving landslides. *Nature Reviews Earth & Environment*, *1*(8), 404-419.

Lappala, E. G., Healy, R. W., & Weeks, E. P. (1987). *Documentation of Computer Program VS2D to Solve the Equations of Fluid Flow in Variably Saturated Porous Media*. Department of the Interior, U.S. Geological Survey.

Lund, J., Medellin-Azuara, J., Durand, J., & Stone, K. (2018). Lessons from California's 2012–2016 Drought. *Journal of Water Resources Planning and Management*, *144*(10), 04018067. https://doi.org/10.1061/(ASCE)WR.1943-5452.0000984

Maceo-Giovanni Angeli, Paolo Gasparetto, Riccardo Massimiliano Menotti, Pasuto, A., & Silvano, S. (1996). A visco-plastic model for slope analysis applied to a mudslide in Cortina d'Ampezzo, Italy. *Quarterly Journal of Engineering Geology and Hydrogeology*, *29*(3), 233–240. https://doi.org/10.1144/GSL.QJEGH.1996.029.P3.06

Macfarlane, D. F. (2009). Observations and predictions of the behaviour of large, slow-moving landslides in schist, Clyde Dam reservoir, New Zealand. *Engineering Geology*, *109*(1), 5–15. https://doi.org/10.1016/j.enggeo.2009.02.005

Mackey, B. H., & Roering, J. J. (2011). Sediment yield, spatial characteristics, and the long-term evolution of active earthflows determined from airborne LiDAR and historical aerial photographs, Eel River, California. *GSA Bulletin*, *123*(7–8), 1560–1576. https://doi.org/10.1130/B30306.1

Malet, J. -P, Maquaire, O., & Calais, E. (2002). The use of Global Positioning System techniques for the continuous monitoring of landslides: application to the Super-Sauze earthflow (Alpes-de-Haute-Provence, France). *Geomorphology, 43*(1), 33–54. https://doi.org/10.1016/S0169-555X(01)00098-8

Malet, J. -P, Van Asch, T. W. J., Van Beek, R., & Maquaire, O. (2005). Forecasting the behaviour of complex landslides with a spatially distributed hydrological model. *Natural Hazards and Earth System Science*, *5*(1), 71–85.

Massey, C. I., Petley, D. N., & McSaveney, M. J. (2013). Patterns of movement in reactivated landslides. *Engineering Geology*, *159*, 1–19. https://doi.org/10.1016/j.enggeo.2013.03.011

Matsuura, S., Asano, S., Okamoto, T., & Takeuchi, Y. (2003). Characteristics of the displacement of a landslide with shallow sliding surface in a heavy snow district of Japan. *Engineering Geology*, *69*(1), 15–35. https://doi.org/10.1016/S0013-7952(02)00245-4

Merriam, R. (1960). Portuguese Bend Landslide, Palos Verdes Hills, California. *The Journal of Geology*, *68*(2), 140–153. https://doi.org/10.1086/626649

Mikkelsen, P. E., & Green, G. E. (2003). Piezometers in fully grouted boreholes (pp. 545–554). Presented at the Field measurements in geomechanics. Retrieved from http://pascal-francis.inist.fr/vibad/index.php?action=getRecordDetail&idt=15388372

Mualem, Y. (1976). A new model for predicting the hydraulic conductivity of unsaturated porous media. *Water Resources Research*, *12*(3), 513–522. https://doi.org/10.1029/WR012i003p00513

Murphy, C., Finnegan, N. J., Oberle, F. J., & Perkins, J. P. (2018). Evidence for a Positive Feedback Between Shallow Groundwater Flow and Shear Failure in an Active Earthflow. *AGU Fall Meeting Abstracts*. Retrieved from http://adsabs.harvard.edu/abs/2018AGUFMEP24B..05M

Nereson, A. L., Olivera, S. D., & Finnegan, N. J. (2018). Field and Remote-Sensing Evidence for Hydro-mechanical Isolation of a Long-Lived Earthflow in Central California. *Geophysical Research Letters*, *45*(18), 9672–9680. https://doi.org/10.1029/2018GL079430

Nereson, A. L., & Finnegan, N. J. (2019). Drivers of earthflow motion revealed by an 80 yr record of displacement from Oak Ridge earthflow, Diablo Range, California, USA. *GSA Bulletin*, *131*(3–4), 389–402. https://doi.org/10.1130/B32020.1

Newmark, N. M. (1965). Effects of Earthquakes on Dams and Embankments. *Géotechnique*, *15*(2), 139–160. https://doi.org/10.1680/geot.1965.15.2.139

Ogden, F. L., Allen, M. B., Lai, W., Zhu, J., Seo, M., Douglas, C. C., & Talbot, C. A. (2017). The soil moisture velocity equation. *Journal of Advances in Modeling Earth Systems*, *9*(2), 1473–1487. https://doi.org/10.1002/2017MS000931

Osawa, H., Matsushi, Y., Matsuura, S., Okamoto, T., Shibasaki, T., & Hirashima, H. (2018). Seasonal transition of hydrological processes in a slow-moving landslide in a snowy region. *Hydrological Processes*, *32*(17), 2695–2707. https://doi.org/10.1002/hyp.13212

Perkins, J. P., Reid, M. E., & Schmidt, K. M. (2017). Control of landslide volume and hazard by glacial stratigraphic architecture, northwest Washington State, USA. *Geology*, *45*(12), 1139–1142. https://doi.org/10.1130/G39691.1

Priest, G. R., Schulz, W. H., Ellis, W. L., Allan, J. A., Niem, A. R., & Niem, W. A. (2011). Landslide Stability: Role of Rainfall-Induced, Laterally Propagating, Pore-Pressure WavesLandslide Stability and Pore-Pressure Waves. *Environmental and Engineering Geoscience*, *17*(4), 315–335. https://doi.org/10.2113/gseegeosci.17.4.315

Pyles, M. R., Mills, K., & Saunders, G. (1987). Mechanics and Stability of the Lookout Creek Earth Flow. *Environmental and Engineering Geoscience*, *xxiv*(2), 267–280. https://doi.org/10.2113/gseegeosci.xxiv.2.267

Reid, M. E. (1994). A Pore-Pressure Diffusion Model for Estimating Landslide-Inducing Rainfall. *The Journal of Geology*, *102*(6), 709–717. https://doi.org/10.1086/629714

Reid, M. E., & Iverson, R. M. (1992). Gravity-driven groundwater flow and slope failure potential: 2. Effects of slope morphology, material properties, and hydraulic heterogeneity. *Water Resources Research*, *28*(3), 939–950. https://doi.org/10.1029/91WR02695

Rempe, D. M., & Dietrich, W. E. (2014). A bottom-up control on fresh-bedrock topography under landscapes. *Proceedings of the National Academy of Sciences*, *111*(18), 6576–6581. https://doi.org/10.1073/pnas.1404763111

Rempe, D. M., & Dietrich, W. E. (2018). Direct observations of rock moisture, a hidden component of the hydrologic cycle. *Proceedings of the National Academy of Sciences*, *115*(11), 2664–2669. https://doi.org/10.1073/pnas.1800141115

Richards, L. A. (1931). Capillary conduction of liquids through porous mediums. *Physics*, *1*(5), 318–333. https://doi.org/10.1063/1.1745010

Richardson, L. F. (1922). *Weather prediction by numerical process,*. Cambridge: University Press.

Roadifer, J. W., Forrest, M. P., & Lindquist, E. S. (2009). Evaluation of shear strength of melange foundation at Calaveras Dam. *Proceedings of U. S. Society for Dams, Annual Meeting and Conference, 29th, on "Managing Our Water Retention Systems, "*, 507–521.

Roering, J. J., Mackey, B. H., Handwerger, A. L., Booth, A. M., Schmidt, D. A., Bennett, G. L., & Cerovski-Darriau, C. (2015). Beyond the angle of repose: A review and synthesis of landslide processes in response to rapid uplift, Eel River, Northern California. *Geomorphology*, *236*, 109–131. https://doi.org/10.1016/j.geomorph.2015.02.013

Schulz, W. H., & Wang, G. (2014). Residual shear strength variability as a primary control on movement of landslides reactivated by earthquake-induced ground motion: Implications for coastal Oregon, U.S. *Journal of Geophysical Research: Earth Surface*, *119*(7), 1617–1635. https://doi.org/10.1002/2014JF003088

Schulz, W. H., Kean, J. W., & Wang, G. (2009). Landslide movement in southwest Colorado triggered by atmospheric tides. *Nature Geoscience*, *2*(12), 863–866. https://doi.org/10.1038/ngeo659

Schulz, W. H., Coe, J. A., Ricci, P. P., Smoczyk, G. M., Shurtleff, B. L., & Panosky, J. (2017). Landslide kinematics and their potential controls from hourly to decadal timescales: Insights from integrating ground-based InSAR measurements with structural maps and long-term monitoring data. *Geomorphology*, *285*, 121–136. https://doi.org/10.1016/j.geomorph.2017.02.011

Schulz, W. H., Smith, J. B., Wang, G., Jiang, Y., & Roering, J. J. (2018). Clayey Landslide Initiation and Acceleration Strongly Modulated by Soil Swelling. *Geophysical Research Letters*, *45*(4), 1888–1896. https://doi.org/10.1002/2017GL076807

Shao, W., Bogaard, T., Bakker, M., & Berti, M. (2016). The influence of preferential flow on pressure propagation and landslide triggering of the Rocca Pitigliana landslide. *Journal of Hydrology*, *543*, 360–372. https://doi.org/10.1016/j.jhydrol.2016.10.015

Simoni, A., Ponza, A., Picotti, V., Berti, M., & Dinelli, E. (2013). Earthflow sediment production and Holocene sediment record in a large Apennine catchment. *Geomorphology*, *188*, 42-53.

Shibasaki, T., Matsuura, S., & Okamoto, T. (2016). Experimental evidence for shallow, slow-moving landslides activated by a decrease in ground temperature. *Geophysical Research Letters*, *43*(13), 6975–6984. https://doi.org/10.1002/2016GL069604

Shobe, C. M., Bennett, G. L., Tucker, G. E., Roback, K., Miller, S. R., & Roering, J. J. (2020). Boulders as a lithologic control on river and landscape response to tectonic forcing at the Mendocino triple junction. *GSA Bulletin*. https://doi.org/10.1130/B35385.1

Sidle, R. C., & Bogaard, T. A. (2016). Dynamic earth system and ecological controls of rainfall-initiated landslides. *Earth-Science Reviews*, *159*, 275–291. https://doi.org/10.1016/j.earscirev.2016.05.013

Singh, D., Ting, M., Scaife, A. A., & Martin, N. (2018). California Winter Precipitation Predictability: Insights From the Anomalous 2015–2016 and 2016–2017 Seasons. *Geophysical Research Letters*, *45*(18), 9972–9980. https://doi.org/10.1029/2018GL078844

Swain, D. L., Langenbrunner, B., Neelin, J. D., & Hall, A. (2018). Increasing precipitation volatility in twenty-first-century California. *Nature Climate Change*, *8*(5), 427-433

Terzaghi, K. (1943). *Theoretical Soil Mechanics*. John Wiley & Sons, Inc.

Torres, R., Dietrich, W. E., Montgomery, D. R., Anderson, S. P., & Loague, K. (1998). Unsaturated zone processes and the hydrologic response of a steep, unchanneled van Lier, Q. de J., Pinheiro, E. A. R., van Lier, Q. de J., & Pinheiro, E. A. R. (2018). An Alert Regarding a Common Misinterpretation of the Van Genuchten α Parameter. *Revista Brasileira de Ciência Do Solo*, *42*. https://doi.org/10.1590/18069657rbcs20170343 catchment. *Water Resources Research*, *34*(8), 1865–1879. https://doi.org/10.1029/98WR01140

Wakabayashi, J. (1992). Nappes, Tectonics of Oblique Plate Convergence, and Metamorphic Evolution Related to 140 Million Years of Continuous Subduction, Franciscan Complex, California. *The Journal of Geology*, *100*(1), 19–40. https://doi.org/10.1086/629569

Wang, G., Suemine, A., & Schulz, W. H. (2010). Shear-rate-dependent strength control on the dynamics of rainfall-triggered landslides, Tokushima Prefecture, Japan. *Earth Surface Processes and Landforms*, *35*(4), 407–416. https://doi.org/10.1002/esp.1937

Wilson, R. C., & Wieczorek, G. F. (1995). Rainfall Thresholds for the Initiation of Debris Flows at La Honda, California. *Environmental and Engineering Geoscience*, *I*(1), 11–27. https://doi.org/10.2113/gseegeosci.I.1.11

Xu, Y., Lu, Z., Schulz, W. H., & Kim, J. (2020). Twelve-Year Dynamics and Rainfall Thresholds for Alternating Creep and Rapid Movement of the Hooskanaden Landslide From Integrating InSAR, Pixel Offset Tracking, and Borehole and Hydrological Measurements. *Journal of Geophysical Research: Earth Surface*, *125*(10), e2020JF005640. https://doi.org/10.1029/2020JF005640

Figure 1.

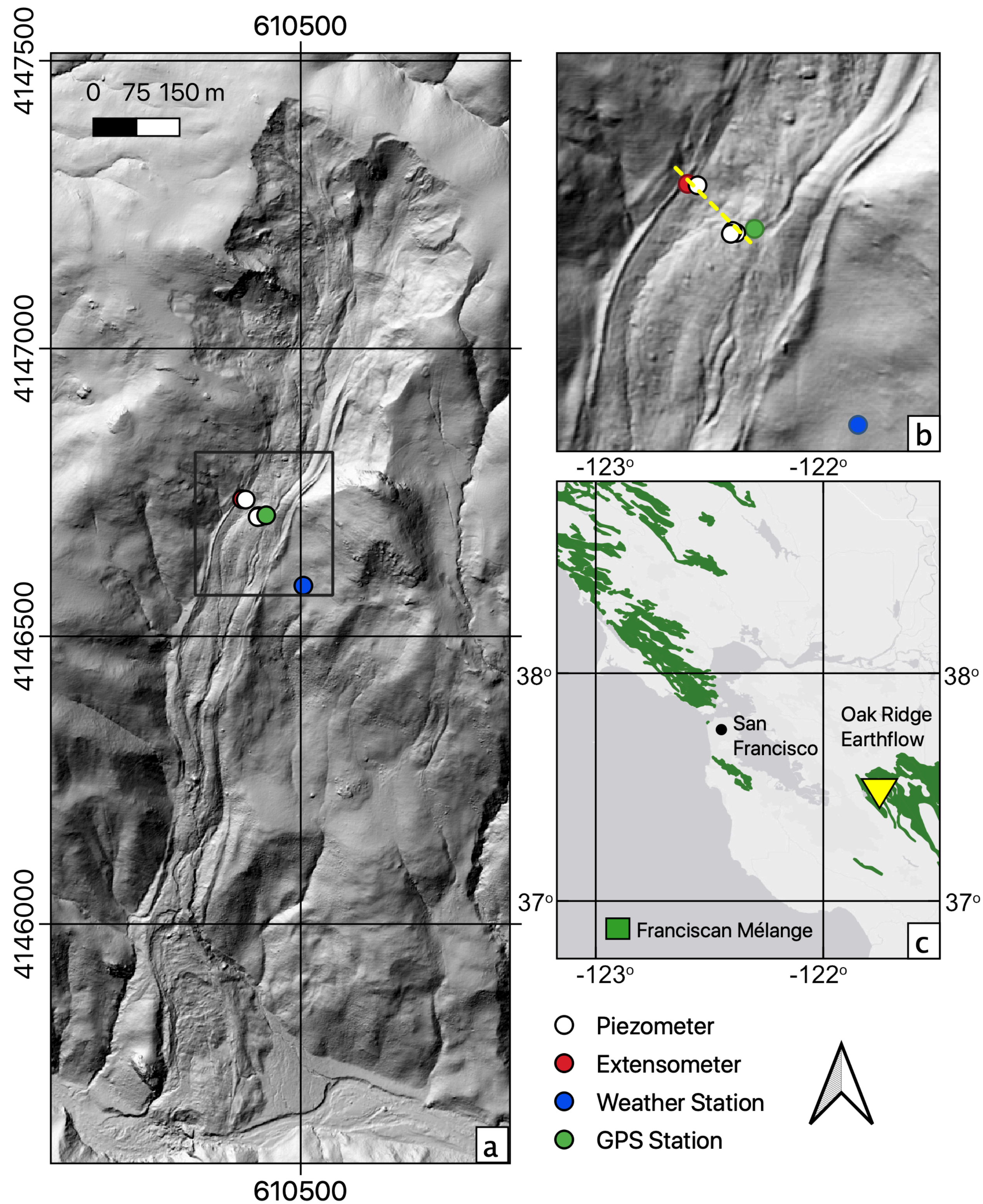
610500
4147500
4147000
4146500
4146000
0 75 150 m
a
610500
b
-123°
-122°
38°
37°
San Francisco
Oak Ridge Earthflow
Franciscan Mélange
c
Piezometer
Extensometer
Weather Station
GPS Station

Figure 2.

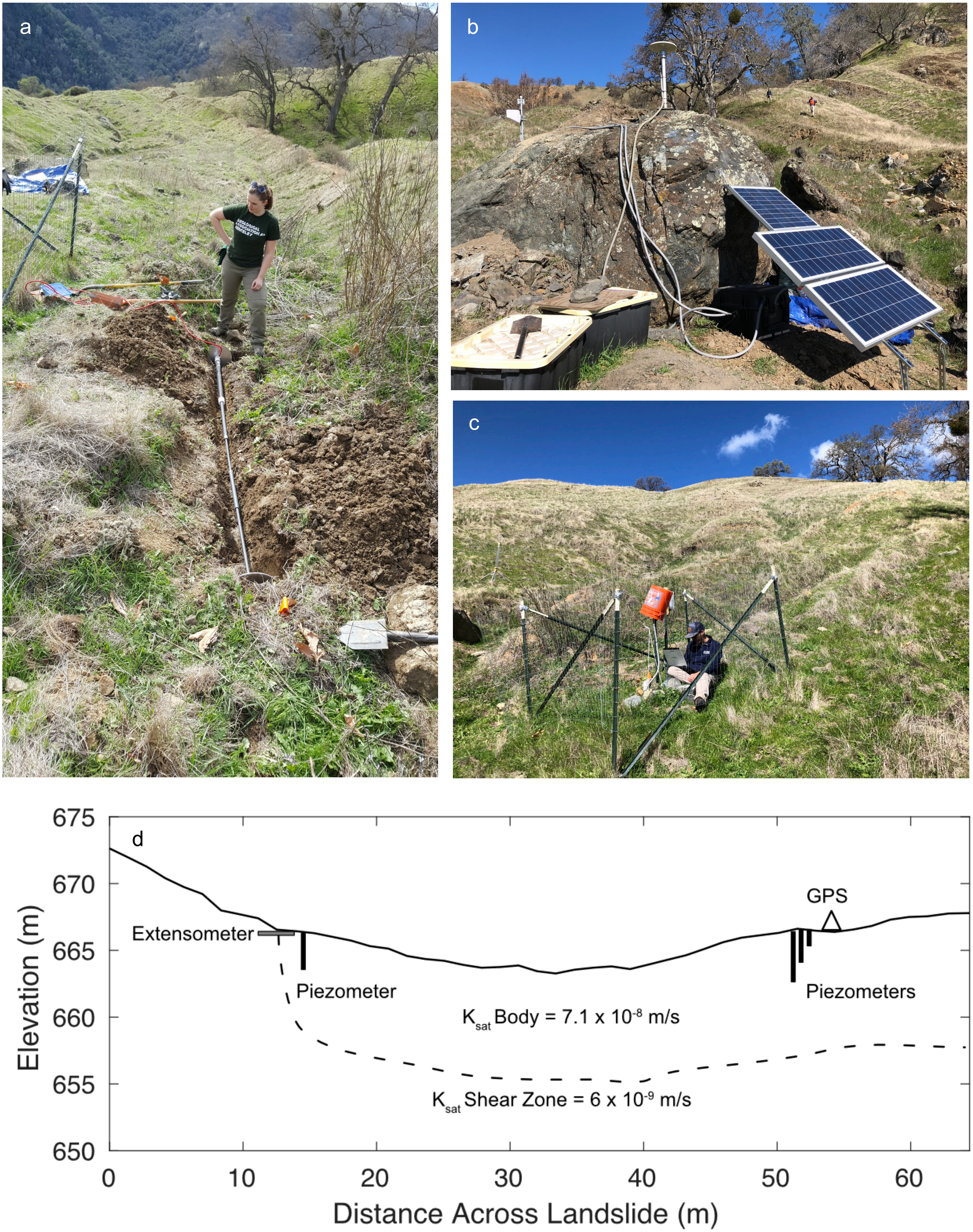
a
b
c
d
675
670
665
660
655
650
Elevation (m)
0
10
20
30
40
50
60
Distance Across Landslide (m)
Extensometer
Piezometer
GPS
Piezometers
K_{sat} Body = 7.1 x 10^{-8} m/s
K_{sat} Shear Zone = 6 x 10^{-9} m/s

Figure 3.

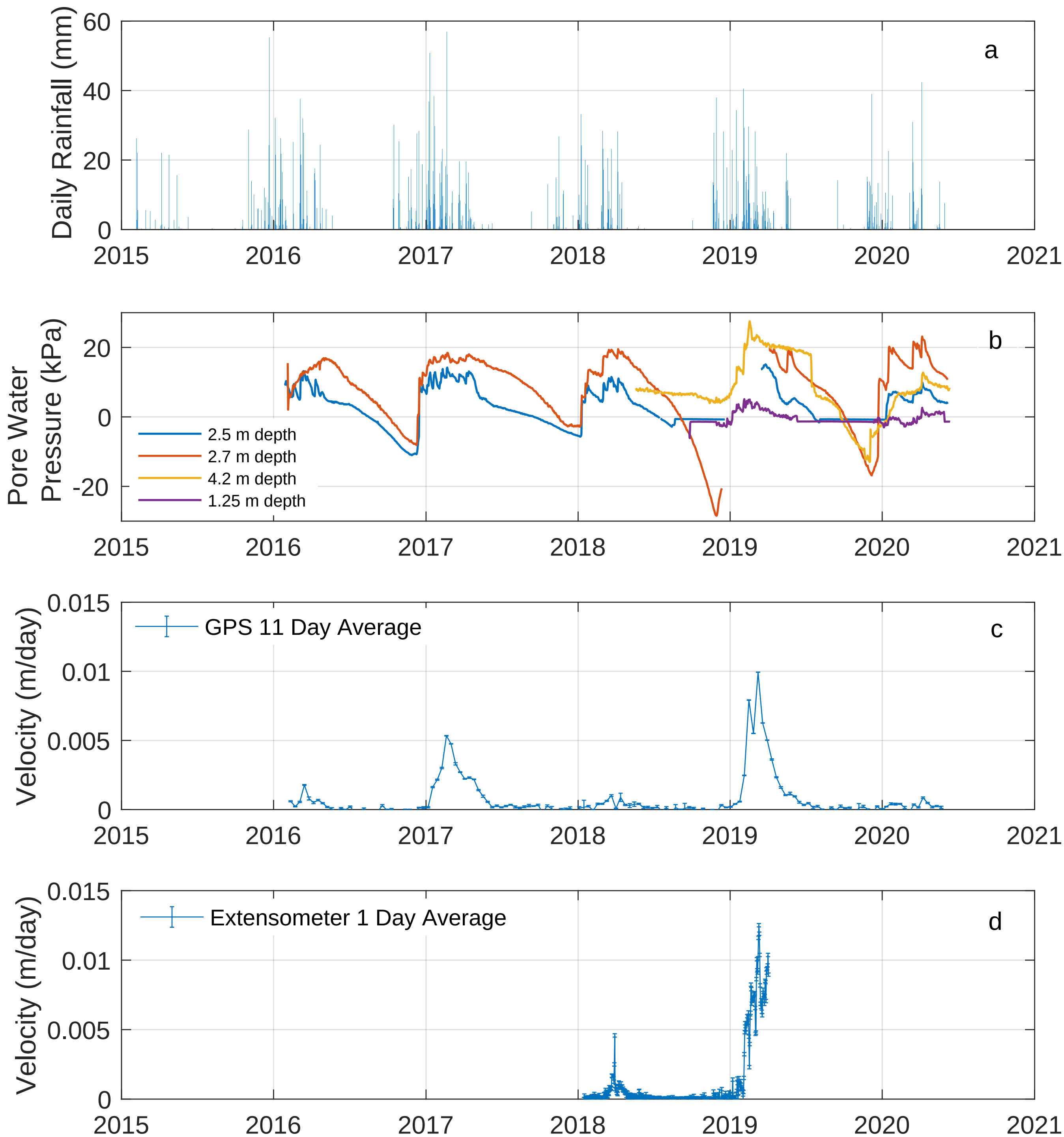

a
Daily Rainfall (mm)
60
40
20
0
2015
2016
2017
2018
2019
2020
2021
b
Pore Water Pressure (kPa)
20
0
-20
2.5 m depth
2.7 m depth
4.2 m depth
1.25 m depth
c
Velocity (m/day)
0.015
0.01
0.005
GPS 11 Day Average
d
Extensometer 1 Day Average

Figure 4.

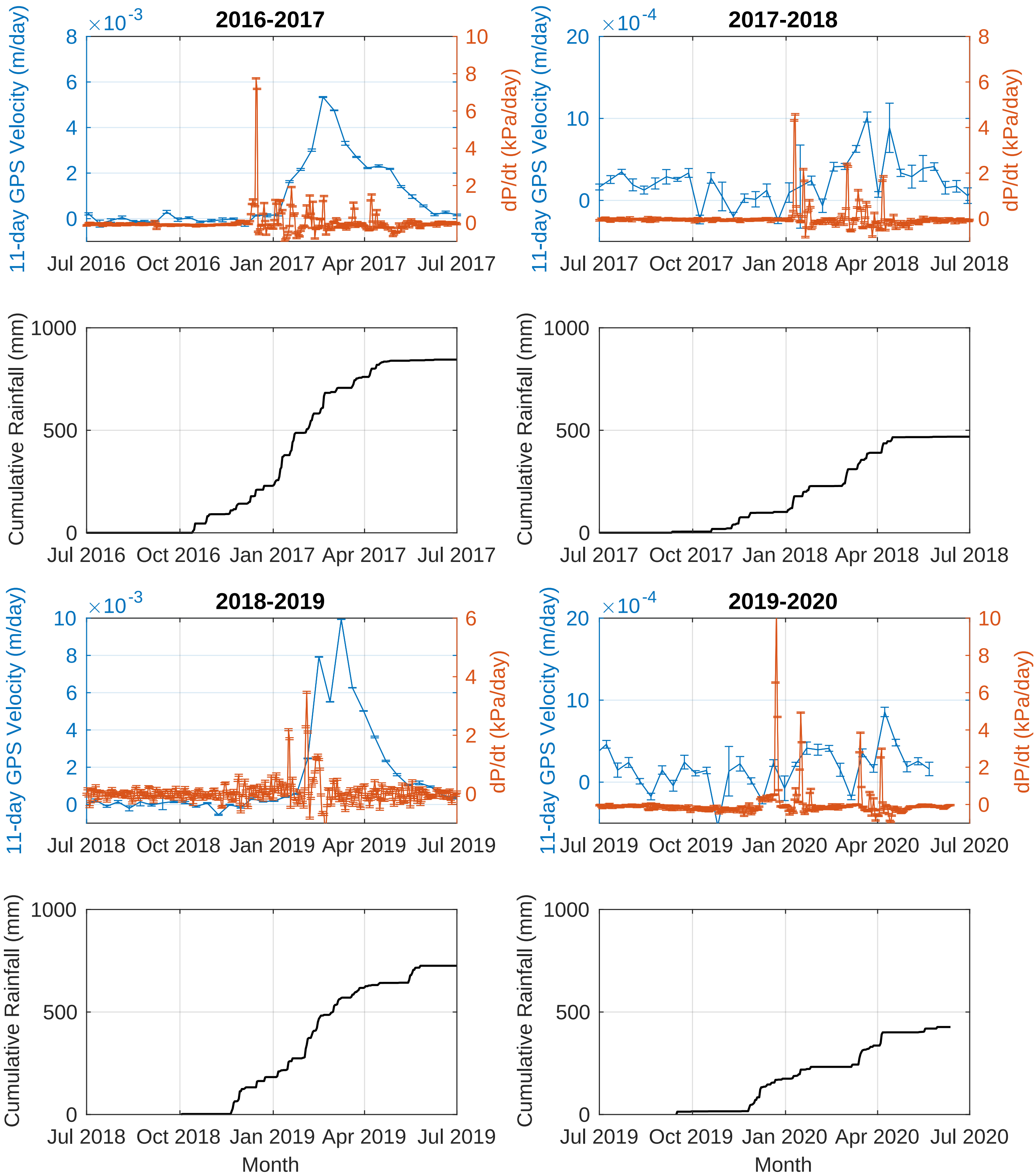

2016-2017
2017-2018
2018-2019
2019-2020
11-day GPS Velocity (m/day)
dP/dt (kPa/day)
Cumulative Rainfall (mm)
×10^-3
×10^-4
Jul 2016 Oct 2016 Jan 2017 Apr 2017 Jul 2017
Jul 2017 Oct 2017 Jan 2018 Apr 2018 Jul 2018
Jul 2018 Oct 2018 Jan 2019 Apr 2019 Jul 2019
Jul 2019 Oct 2019 Jan 2020 Apr 2020 Jul 2020
Month

Figure 5.

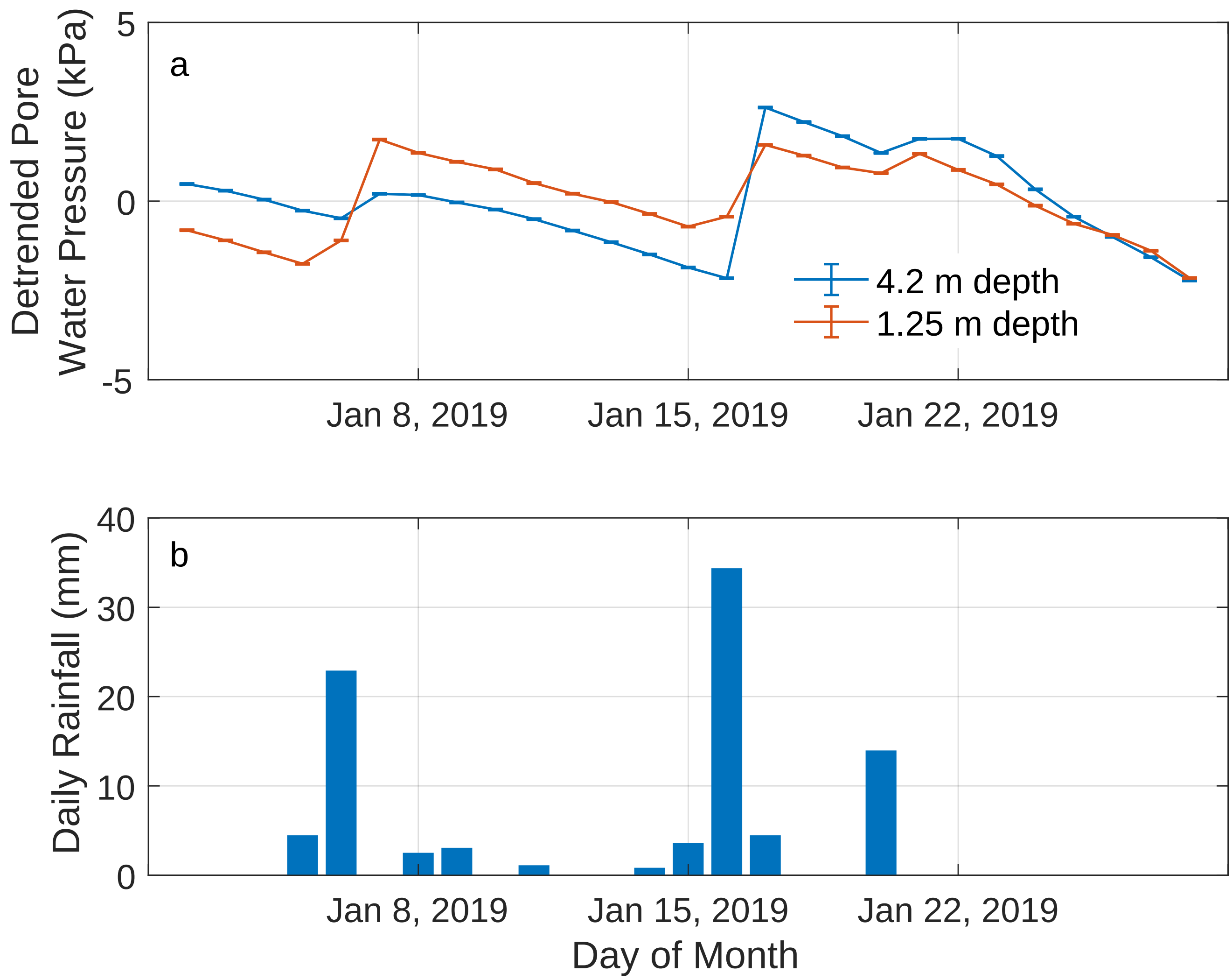

Detrended Pore
Water Pressure (kPa)
5
0
-5
a
4.2 m depth
1.25 m depth
Jan 8, 2019
Jan 15, 2019
Jan 22, 2019
Daily Rainfall (mm)
40
30
20
10
0
b
Jan 8, 2019
Jan 15, 2019
Jan 22, 2019
Day of Month

Figure 6.

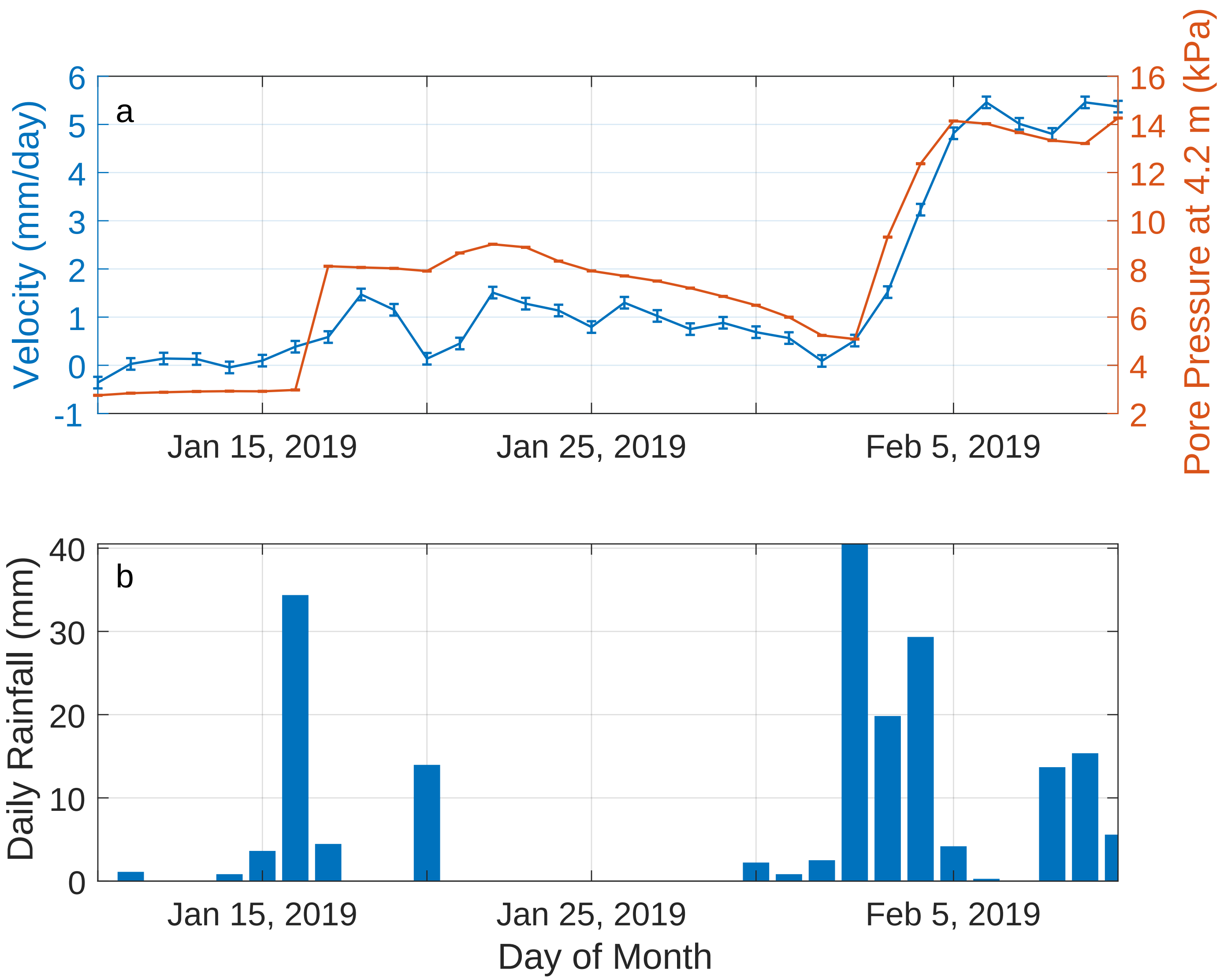

a
Velocity (mm/day)
Pore Pressure at 4.2 m (kPa)
Jan 15, 2019
Jan 25, 2019
Feb 5, 2019
b
Daily Rainfall (mm)
Day of Month

Figure 7.

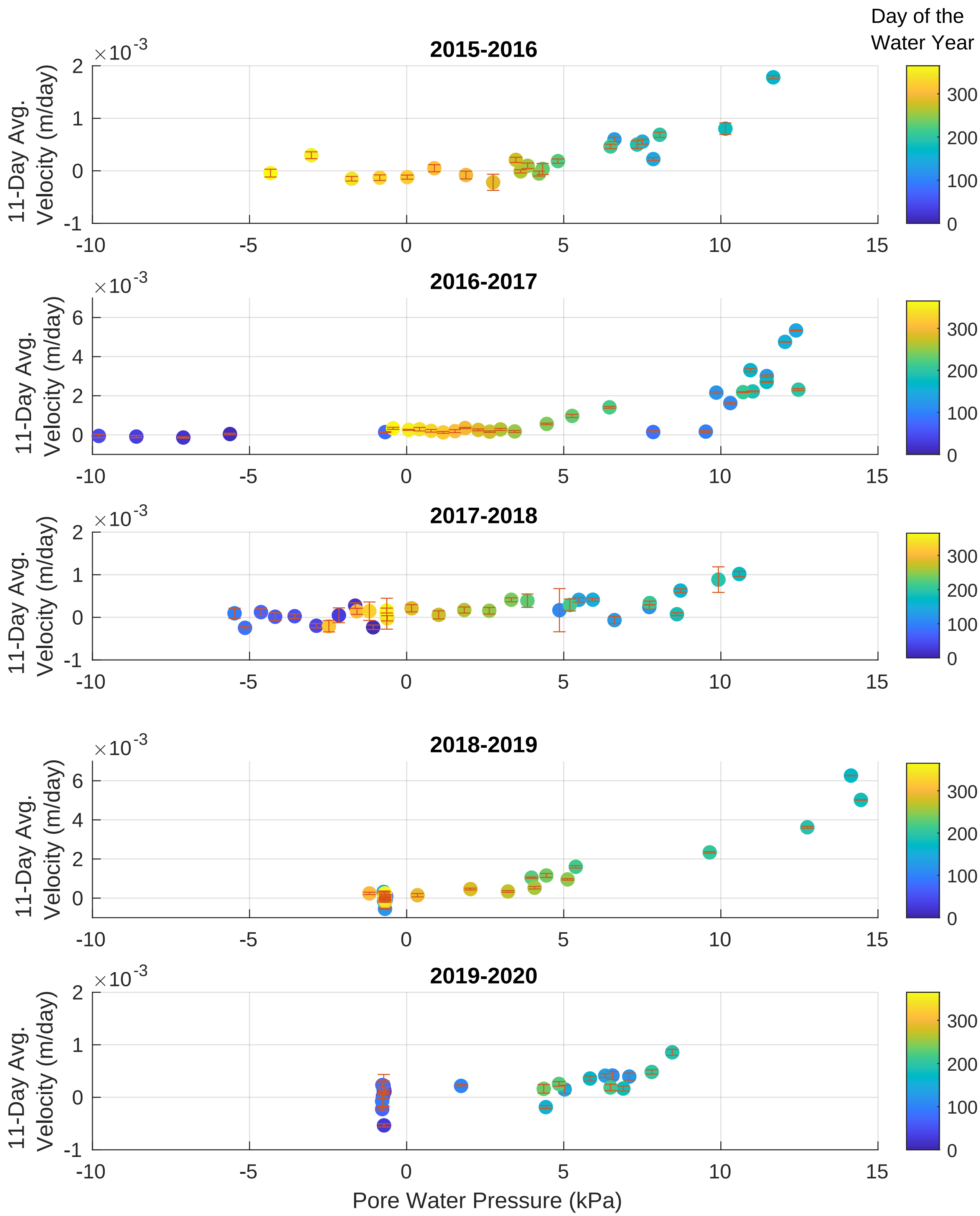
Day of the Water Year
2015-2016
2016-2017
2017-2018
2018-2019
2019-2020
×10^-3
11-Day Avg. Velocity (m/day)
Pore Water Pressure (kPa)
-10
-5
0
5
10
15
0
100
200
300

Figure 8.

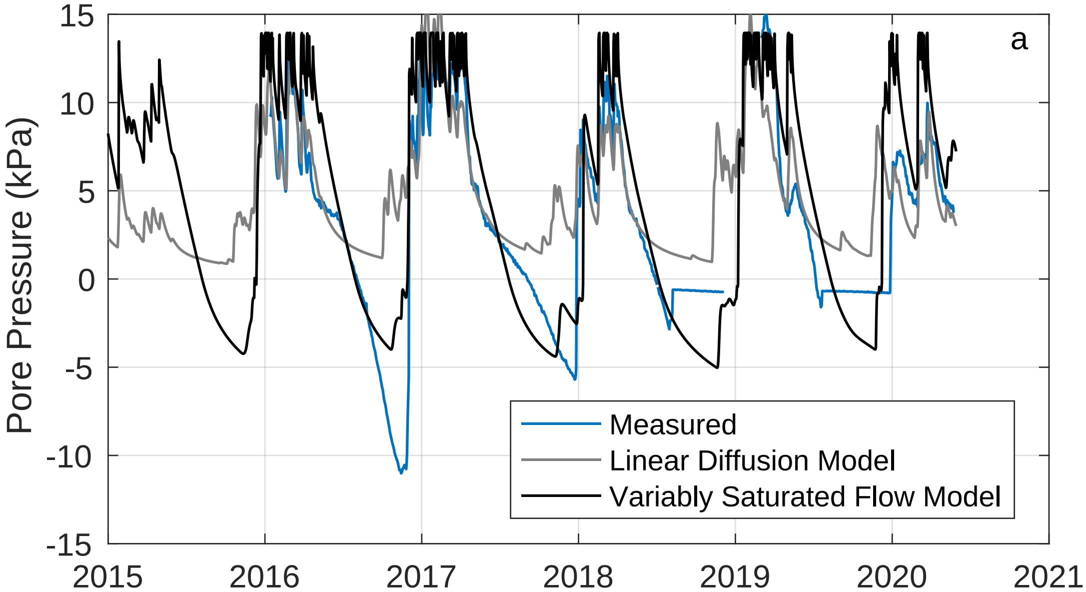

a
Pore Pressure (kPa)
Measured
Linear Diffusion Model
Variably Saturated Flow Model
15
10
5
0
-5
-10
-15
2015
2016
2017
2018
2019
2020
2021

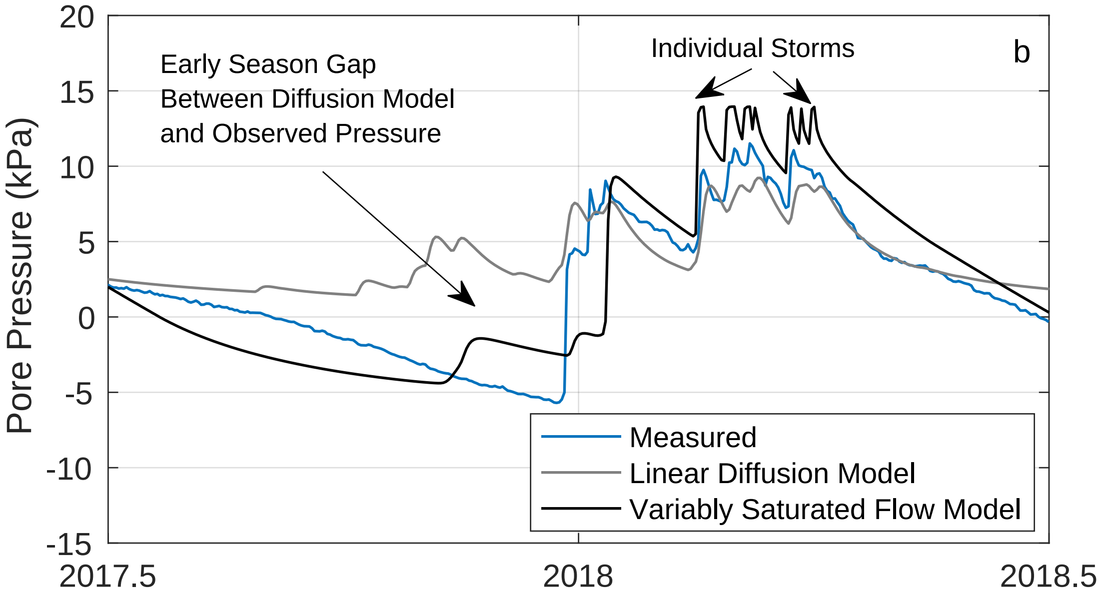

b
Early Season Gap
Between Diffusion Model
and Observed Pressure
Individual Storms
Pore Pressure (kPa)
Measured
Linear Diffusion Model
Variably Saturated Flow Model
20
15
10
5
0
-5
-10
-15
2017.5
2018
2018.5

Figure 9.

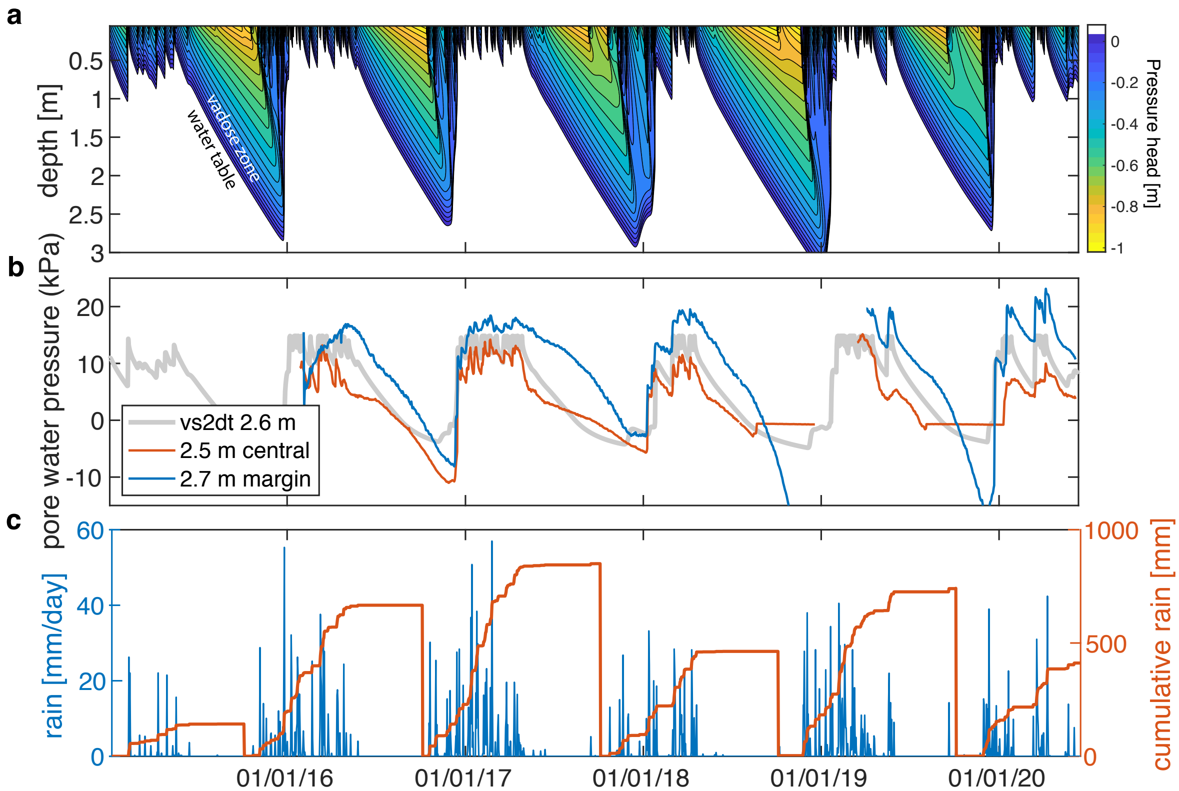
a
depth [m]
0.5
1
1.5
2
2.5
3
vadose zone
water table
Pressure head [m]
0
-0.2
-0.4
-0.6
-0.8
-1
b
pore water pressure (kPa)
20
10
0
-10
vs2dt 2.6 m
2.5 m central
2.7 m margin
c
rain [mm/day]
60
40
20
0
cumulative rain [mm]
1000
500
0
01/01/16
01/01/17
01/01/18
01/01/19
01/01/20

Figure 10.

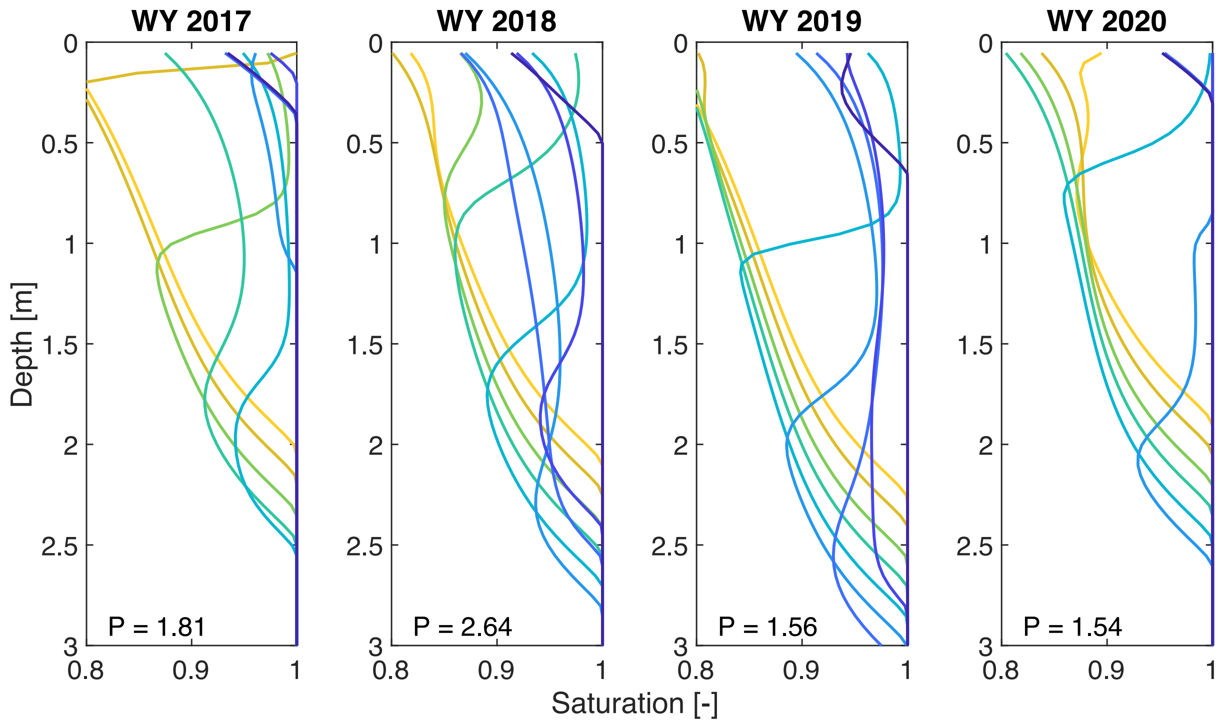
WY 2017
WY 2018
WY 2019
WY 2020
Depth [m]
Saturation [-]
P = 1.81
P = 2.64
P = 1.56
P = 1.54
0
0.5
1
1.5
2
2.5
3
0.8
0.9
1

Figure 11.

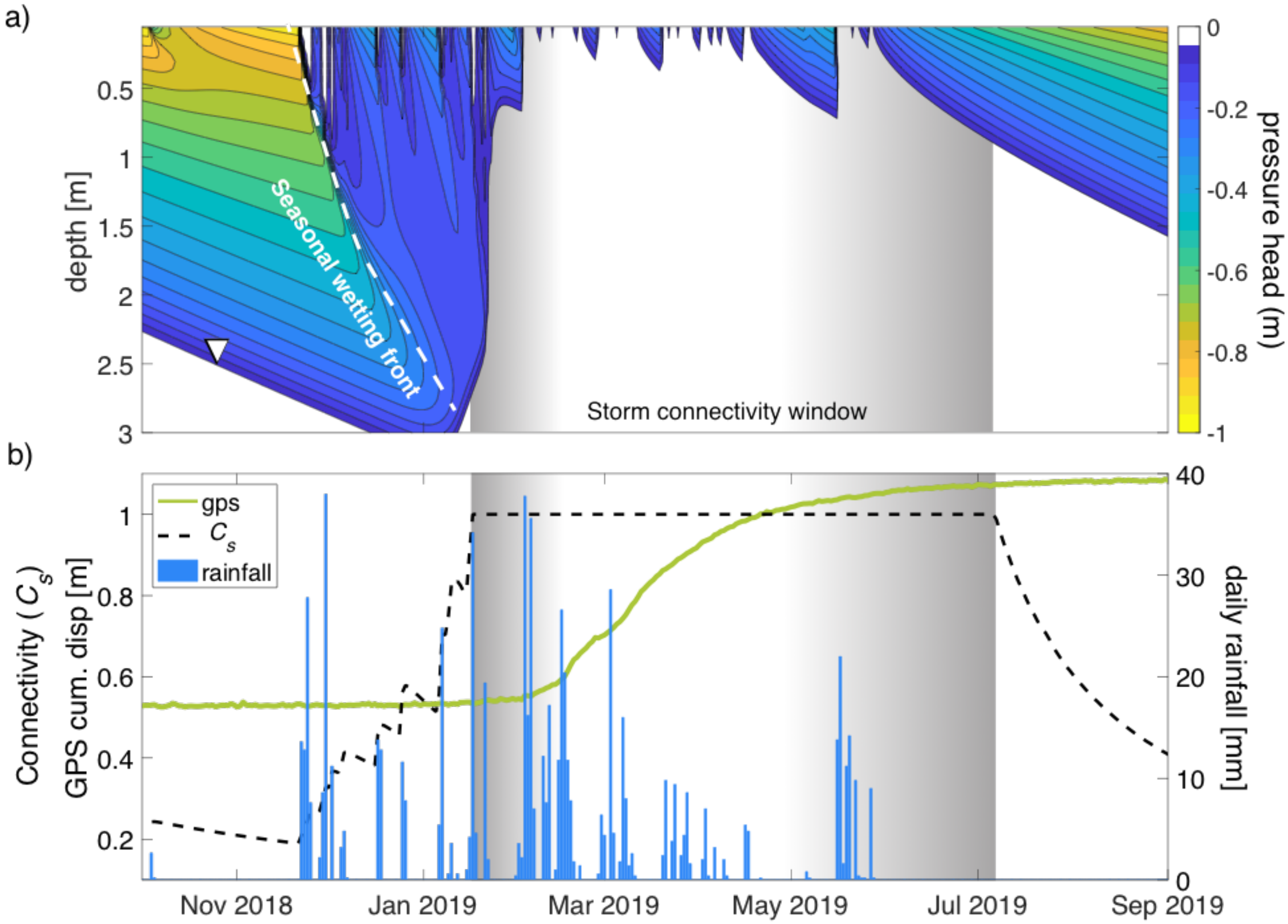
a)
b)
depth [m]
0.5
1
1.5
2
2.5
3
Seasonal wetting front
Storm connectivity window
pressure head (m)
0
-0.2
-0.4
-0.6
-0.8
-1
gps
C_s
rainfall
Connectivity (C_s)
GPS cum. disp [m]
daily rainfall [mm]
0.2
0.4
0.6
0.8
1
0
10
20
30
40
Nov 2018
Jan 2019
Mar 2019
May 2019
Jul 2019
Sep 2019

Figure 12.

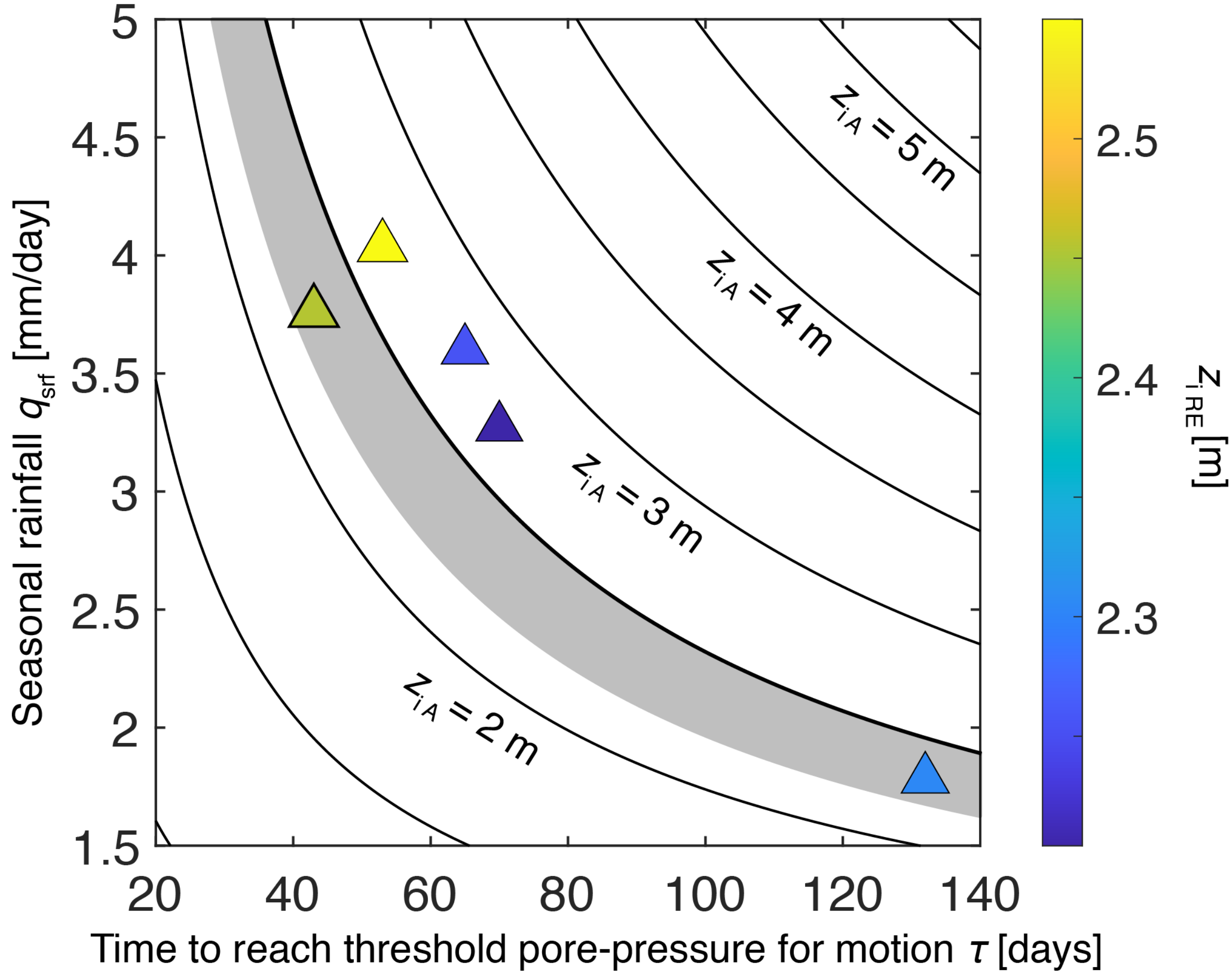

5
4.5
4
3.5
3
2.5
2
1.5
20
40
60
80
100
120
140
Seasonal rainfall q_{srf} [mm/day]
Time to reach threshold pore-pressure for motion τ [days]
z_{iA} = 5 m
z_{iA} = 4 m
z_{iA} = 3 m
z_{iA} = 2 m
2.5
2.4
2.3
z_{iRE} [m]